Phosphidation-Free Synthesis of Ni x Co y P on Nanostructured N,S,P-Doped Carbon Networks as Self-Supported Multifunctional Electrocatalysts

Sarra Knani, Myriam Tauk, Perla Hajjar, Marie-agnès Lacour, Masoud Shahrokhi, Christine Canaff, Cláudia Morais, Sophie Morisset, Patrice Huguet, Didier Cot, et al.

To cite this version:

Sarra Knani, Myriam Tauk, Perla Hajjar, Marie-agnès Lacour, Masoud Shahrokhi, et al.. Phosphidation-Free Synthesis of Ni x Co y P on Nanostructured N,S,P-Doped Carbon Networks as Self-Supported Multifunctional Electrocatalysts. Small Structures, 2024, 2400276, pp.1-21. 10.1002/sstr.202400276 . hal-04755253

HAL Id: hal-04755253
https://hal.science/hal-04755253v1

Phosphidation-free Synthesis of Ni_xCo_yP on Nanostructured N,S,P-Doped Carbon Networks as Self-Supported Multifunctional Electrocatalysts

Sarra Knani‡, Myriam Tauk‡, Perla Hajjar‡, Marie-Agnès Lacour, Masoud Shahrokhi, Christine Canaff, Cláudia Morais, Sophie Morisset, Patrice Huguet, Didier Cot, Bertrand Rebiere, Erwan Oliviero, Valerie Bonniol, Julien Cambedouzou, Mikhael Bechelany, Sophie Tingry, K. Boniface Kokoh, Teko W. Napporn, Hazar Guesmi, David Cornu, and Yaovi Holade**

S. Knani, M. Tauk, P. Hajjar, P. Huguet, D. Cot, V. Bonniol, J. Cambedouzou, M. Bechelany, S. Tingry, D. Cornu, Y. Holade
Institut Européen des Membranes, IEM, UMR 5635, Univ Montpellier, ENSCM, CNRS, 34090 Montpellier, France
‡ These authors contributed equally
Corresponding author: yaovi.holade@enscm.fr (Y.H.)

M.-A. Lacour
ChemLab, ENSCM, 34296 Montpellier, France

M. Shahrokhi, B. Rebiere, E. Oliviero, H. Guesmi
Institut Charles Gerhardt Montpellier, ICGM, UMR 5253, Univ Montpellier, ENSCM, CNRS, 34090 Montpellier, France
Corresponding author: hazar.guesmi@enscm.fr (H.G.)

C. Morais, C. Canaff, S. Morisset, K.B. Kokoh, T.W. Napporn
IC2MP, UMR-CNRS 7285, Université de Poitiers, 86073 Poitiers Cedex 9, France

E. Oliviero
MEA Platform Université de Montpellier, 34090 Montpellier, France

C. Canaff, C. Morais, P. Huguet, J. Cambedouzou, S. Tingry, K.B. Kokoh, T.W. Napporn, H. Guesmi, D. Cornu, Y. Holade
French Research Network on Hydrogen (FRH2), Research Federation No. 2044 CNRS, BP 32229, 44322 Nantes CEDEX 3, France, https://frh2.cnrs.fr/

M. Bechelany
Functional Materials Group, Gulf University for Science and Technology (GUST), Mubarak Al-Abdullah 32093, Kuwait

Keywords: density functional theory, electrosynthesis, hydrogen evolution, 5-hydroxymethylfurfural, transition metal phosphides

Abstract

The synthesis of supported multi-element transition metal phosphides (TMPs) to exploit the synergistic interplay between electronic and geometric effects resulting from the presence of different metals in the material and the arrangement of heterogeneous atoms is pivotal for reducing metal content while offering multiple active sites. However, the integration of Ni, Co and P, for example, into a nanostructured carbon network to develop self-supporting Ni_xCo_yP bimetallic phosphides is limited by several factors, including the synthesis and the discrepancy between the crystal structure of the respective monometallic phosphides. Moreover, conventional synthesis of supported TMPs often separates nanoparticles, support and phosphidation steps, which do not allow tailoring of physical and catalytic properties *via* particle-support, electronic and geometric interactions. Herein, we present an innovative solid-state, *ex situ* phosphidation-free approach tailored to synthesize a library of self-supporting Ni_xCo_yP TMPs in N,S,P-modified nanostructured carbon networks generated together with Ni_xCo_yP particles. Extensive multivariate characterization validates the unique properties of Ni_xCo_yP bimetallic materials with enhanced electrocatalytic performance for the hydrogen evolution reaction and the selective electroconversion of biomass-derived 5-HMF (5-hydroxymethylfurfural) to value-added FDCA (2,5-furandicarboxylic acid) with 90-100% faradaic efficiency. Overall, the synthesis expands the possibilities for tailoring the microstructure of supported TMPs for improved physical/catalytic properties.

1. Introduction

The economic viability of hybrid hydrogen production depends on the nature and structure of the electrode materials as well as other constituents of electrolyzers. Recently, major advances in the design of electrolyzer components have prompted the development of low-cost metals as electrode materials for electrochemical biomass conversion into chemicals and fuels of interest.[1] A practical approach to achieving efficient activity and stability is to modify the microstructure of the active metal(s) with heteroatoms such as phosphorus (P), to regulate electron density delocalization (donor-acceptor capacity as a function of the electronic environment created by the microstructure).[2] This ensures that designed electrocatalysts have the right structure, morphology and surface energy to drive the electrocatalytic reaction to specific products with more exposed active sites, resulting in decent efficiency. Conventionally, the phosphidation process is carried out only for the metal part[2a,2d,3] and not simultaneously during the synthesis of the support, which does not leverage the significant modification of the particle support by P to enhance catalytic performance. Indeed, P can modify the valence state of Ni and Co as well as the carbon-based supports, thus promoting the adsorption/desorption of reactants and/or intermediates owing to diverse structural and electronic properties that synergistically enhance the performance.[2e,4] Other unsupported transition metal phosphides (TMPs) materials such as Mo-Ru-P[5] have been reported for electrocatalytic tasks. Traditionally, pre-made carbon substrates (Vulcan-XC72 (carbon black), CNTs (carbon nanotubes), rGO (reduced graphene oxide), metal foams, etc.) are mixed with metal particles due to their high specific surface area and good electrical conductivity, which often results in a loss of active sites as the metal species are not strongly attached to the support.[2e,3b,4a,5b,6] Thus, although unsupported electrocatalysts have attracted significant interest as electrode materials in electrocatalysis, the self-supporting approach should improve metal-support interaction. Self-supported electrocatalysts offer other advantages over conventional materials: abundant active sites thanks to better catalyst dispersion, improved electroactive surface, and fast charge transfer and mass transport kinetics.[17]

Embedding Ni and Co in the same self-supported bimetallic phosphides (Ni_xCo_yP) within nanostructured N,S,P-modified carbon networks has been challenging, as the crystallographic arrangement of the elements in the respective monometallic phosphides is radically different. Specifically, Ni_2P adopts a hexagonal structure, while CoP exhibits an orthorhombic structure. Thus, during a self-supporting approach, introducing phosphorus can lead either to segregated monometallic phosphide phases, or to a new bimetallic phosphide crystal structure distinct from or linked to Ni_2P and CoP. Consequently, this interaction can induce a microstructural change in the material, favoring one crystal structure over another. For example, if the interaction between phosphorus and nickel atoms predominates, the material may favor a hexagonal crystal structure similar to that of Ni_2P. Conversely, if the interaction between phosphorus and cobalt atoms is stronger, the alloy may adopt an orthorhombic crystal structure resembling CoP. Thus, depending on the synthesis approach and the distinct crystal structures of the individual components and their respective phosphides, various crystallographic structures have been proposed for Co-Ni-P, amorphous or disordered phases, which can appear under rapid quenching or non-equilibrium conditions.[6-7] Moreover, ordered phases such as the L12 and L10 structures were considered, characterized by specific arrangements of Co and Ni atoms within a face-centered cubic (FCC) or tetragonal lattice, respectively.[8] Furthermore, intermediate phases or metastable structures may also appear, exhibiting unique arrangements distinct from those of pure elements or binary compounds.[9]

The above potential structural difference highlights the complexity of *ex situ* phosphidation-free synthesis of Ni_xCo_yP on N,S,P-modified nanostructured carbon networks as self-supporting electrocatalysts, and underscores the need for developing an innovation single step synthesis method. The adsorption free energy of the electroactive species and the density of state (DOS) have been calculated by density functional theory (DFT) on models of Ni_2P, CoP and NiCo,[2b,10] not for the electrocatalytic oxidation of 5-Hydroxymethylfurfural (5-HMF). Spectroelectrochemistry (*in situ* infrared reflectance spectroscopy coupled with electrochemistry) that provides crucial information regarding the adsorbed surface species and reaction products at the electrode-electrolyte interface,[11] have not yet been implemented with DFT to study 5-HMF electrooxidation. Hence, the coupling of both techniques is recommended to sort out the elementary steps of the electrochemical reactions and to define the active sites and the rate determining step. To date, thermodynamic data for Pathway A (Scheme 1) have been reported by ab initio calculations.[12] We note that the conversion of cellulosic biomass into useful chemicals is a key goal in green chemistry.[1,13] Scheme 1 outlines the electrocatalytic oxidation pathways of 5-HMF, emphasizing the preservation of C-C bonds for valuable bio-products.[1c,13-14] Two electrocatalytic pathways diverge in the oxidation of 5-HMF. Pathway A initially oxidizes the aldehyde group to form 5-hydroxymethyl-2-furan carboxylic acid (HMFCA) or its anhydride, leading to 2,5-furandicarboxylic acid (FDCA) *via* intermediates. Pathway B oxidizes the hydroxymethyl group to form 2,5-diformylfuran (DFF) or furan-2,5-dicarbaldehyde (FDA), also yielding FDCA. These electrocatalytic processes, mediated by electron transfer reactions, are still debated since the intuitive Pathway A (C-H activation)[15] is not valid for some organic molecules electrooxidation where the O-H activation is prevailing.[15c,16] Thus, for a better clarification of the 5-HMF oxidation mechanism, we propose in this work a detailed DFT study using Ni_2P as a model electrocatalyst comparing the data with those obtained by spectroelectrochemistry, for the first time to our knowledge. To address the above experimental challenges, we report herein a new sacrificial and *ex situ* phosphidation-free synthesis strategy to develop Ni_xCo_yP (as electrocatalytically active species) on nanostructured N,S,P-modified carbon networks (as support for electronic conduction and the metal loading reduction). Our novel experimental and theoretical approach relies on a set of *in-situ* and *ex-situ* physicochemical, electrochemical, spectroelectrochemical, DFT and chromatography investigations for two model reactions, the electrooxidation of 5-HMF and the hydrogen evolution reaction (HER) for possible biomass electro-valorization systems.[1a,1b]

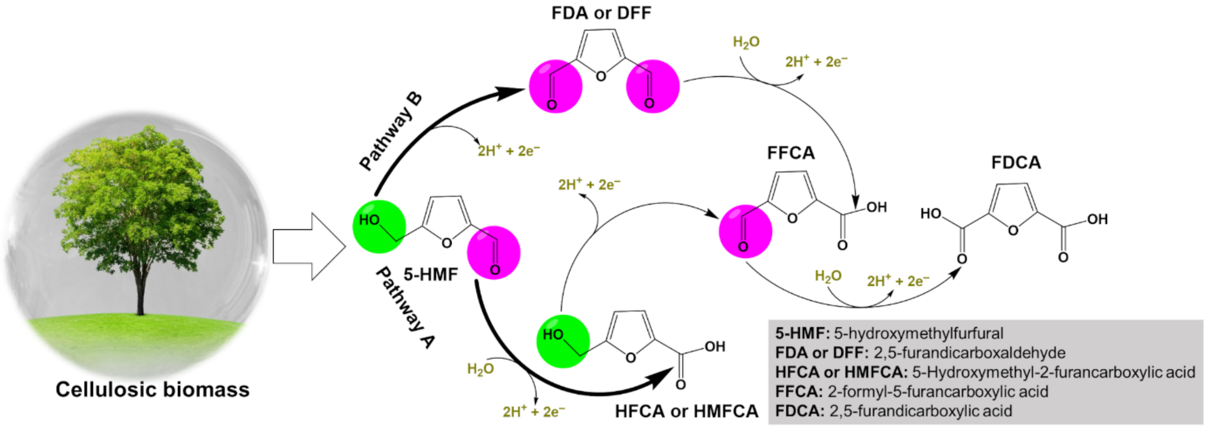

Scheme 1. Sketch of electrochemical synthesis of FDCA (right side) from abundant biomass (left side) based 5-HMF, selectively oxidized by two main reaction pathways, written in acidic forms (adapted from Ref.[17] under a CC BY 4.0 license, Licensee MDPI, Basel, Switzerland).

2. Results and Discussion

2.1. Synthesis and Physicochemical Characterization

2.1.1. Structural, Compositional and Textural Characterization

Based on our previous studies on nickel sulfides,[18] we hypothesized that chemical polymerization combined with the carbothermal reducing atmosphere generated by the decomposition of polyaniline (PANI) and the continuous flow of nitrogen gas at 900 °C should allow sufficient diffusion of Ni, Co, and P species to form a single nanostructured bimetallic phosphide phase (Ni_xCo_yP). Table S1 shows the synthesis conditions for the different Ni/Co compositions. We have chosen PANI as the source of carbon and nitrogen to enable an *in situ* generation of the electrocatalyst support. However, it is still unknown which monometallic phosphide structure (Ni_2P (hexagonal), CoP (orthorhombic)) the bimetallic phosphide Ni_xCo_yP will follow if we exclude segregated monometallic phosphide phases onto the *in-situ* generated N,S,P-modified carbon networks.

Scheme 2 outlines the proposed synthetic approach for the preparation of self-supporting heterostructure electrocatalysts consisting of a matrix of Ni, Co, P and C, using the crystal structures of Ni_2P and CoP as key reference points for understanding how phosphorus affects the microstructure of bimetallic phosphides. Compared to existing methods,[2a,2d,3,5,19] our innovative solid-state, *ex-situ*, phosphidation-free approach enables the controlled, simultaneous and single-step synthesis of a tunable amount of electrocatalytically active species of Ni_xCo_yP particles on N,S,P-modified nanostructured carbon networks as particle support for electronic conduction and metal charge reduction (targeting Ni+Co metal loading below 50 wt%). More specifically, the presence of Ni, Co, P and C precursors in the polymerized raw material offers a number of advantages: (i) eliminating the need for a prefabricated electrocatalyst support, (ii) avoiding the addition of an external P source during carbothermal reduction (e.g., eliminating the risky handling of bulk phosphorus materials), and (iii) eliminating the addition of carbon black powder during electrocatalytic ink preparation. Indeed the traditional synthesis methodologies for TMPs consist of an *ex-situ* phosphidation processes,[2a,2d,3,19a-e] whereby the metallic species (metals, hydroxides, oxides, carbonates, etc.) obtained by different methods (electroreduction,[19a] hydrothermal,[19b] solvothermal[19e]) are first formed. A subsequently phosphorization processes is performed using different P sources during: (i) liquid-phase reactions (based on trioctylphosphine, triphénylphosphine, etc.),[19a,19f] (ii) solid-gas reactions (based on phosphorus vapor[19d] or PH_3 formed during the decomposition of P(V) precursors (NaH_2PO_2, $NH_4H_2PO_2$, etc.)[19b-d]) that are often combined with thermal treatment under mild temperature (300 °C under inert gas (Ar, N_2)),[19b] and (iii) solid-state reactions at high reaction temperatures (800-1200 °C under inert gas (Ar, N_2)).[19c,20] Hence, as recently emphasized by Mazur et al.[20b], our present methodology enables to minimize the handling of corrosive, flammable, and hazardous organic phosphines while simplifying the synthesis procedure for scale-up potentiality in obtaining supported TMPs-based electrocatalysts. Herein, PANI was obtained from the polymerization of aniline initiated by $(NH_4)_2S_2O_8$ (ammonium persulfate, APS) as oxidant in H_3PO_4 as acid dopant and phosphorus source. During the synthesis, detailed in the Experimental section, the polymerization of aniline was monitored by the transition of the solution color from green to green-black, which appeared 15 minutes after the start and persisted until the end of the synthesis. It remains to be seen whether *in situ* phosphidation during heat treatment of the materials leads to the formation of crystallized Ni-Co phosphides.

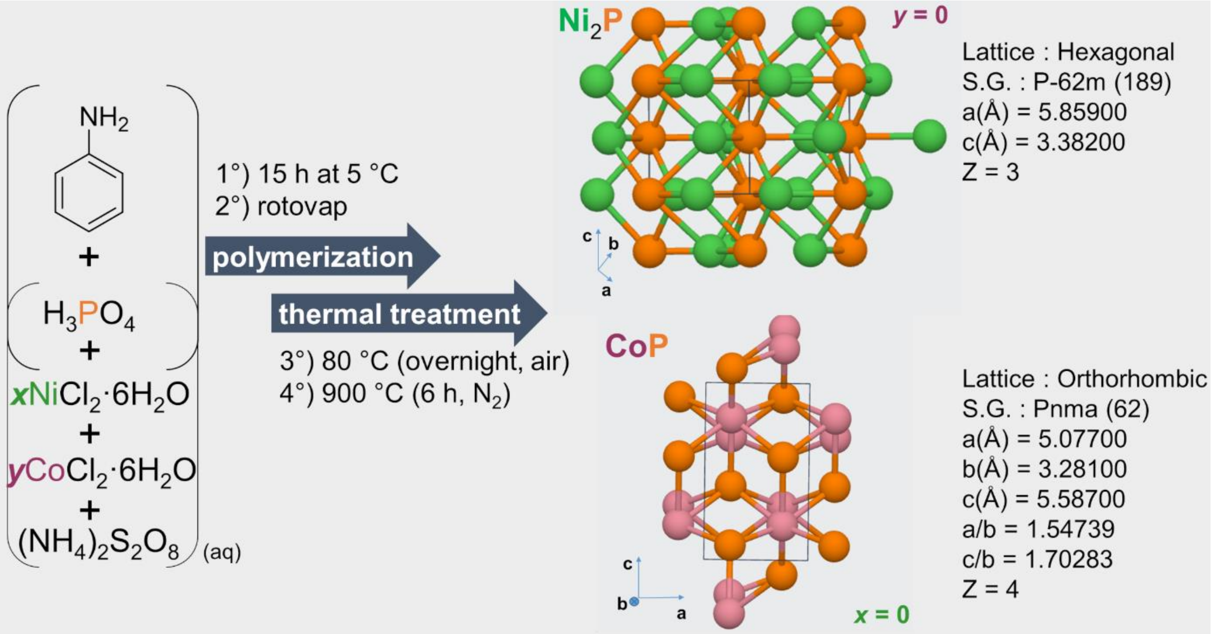

Scheme 2. Outline of the developed synthesis: The structures correspond to the monometallic situation, and the aim is to discover which structure the bimetallic will evolve towards.

We first used X-ray diffraction (XRD) to study the crystal structure of the synthesized phosphide materials. Overall, the XRD results in Figure 1a show well-defined peaks (except for PANI-Co), confirming the high crystallinity of the materials. Monometallic PANI-Ni shows a Ni_2P pattern characteristic of a hexagonal structure (ICDD #03-065-1989) and space group P62m (lattice parameters a = b = 5.859 Å, and c = 3.382 Å) with the main diffraction peaks at 30.5°, 31.7°, 35.3°, 40.7°, 44.5°, 47.3°, 54.1°, and 54.9°. For monometallic PANI-Co, the diffractogram is characteristic of CoP with an orthorhombic crystal structure (ICDD #00-006-0663) and the space group Pnma (lattice parameters a = 5. 070 Å, b = 3.281 Å, and c = 5.587 Å) with the main diffraction peaks at 31.5°/31.9°, 35.2°, 36.2°/36.6°, 46.1°, 48.0°, 52.2°, 55.9°, and 56.7°. In addition, the determined crystallite size (L_V) estimated from the Scherrer's law was 32 and 64 nm for PANI-Ni (Ni_2P hexagonal structure) and PANI-Co (CoP orthorhombic structure), respectively. Interestingly, P is initially in substantial excess (the molar ratio of (H_3PO_4)/($MCl_2·6H_2O$, M = Ni, Co) being 5.5), so the difference in crystal structure between PANI-Ni (Ni_2P) and PANI-Co (CoP) materials is unlikely to be due to P deficiency.[21] The above results confirm the effectiveness of polymerization with *in situ* phosphidation for the rational design of nickel-cobalt phosphide materials with different microstructures (Scheme 2).

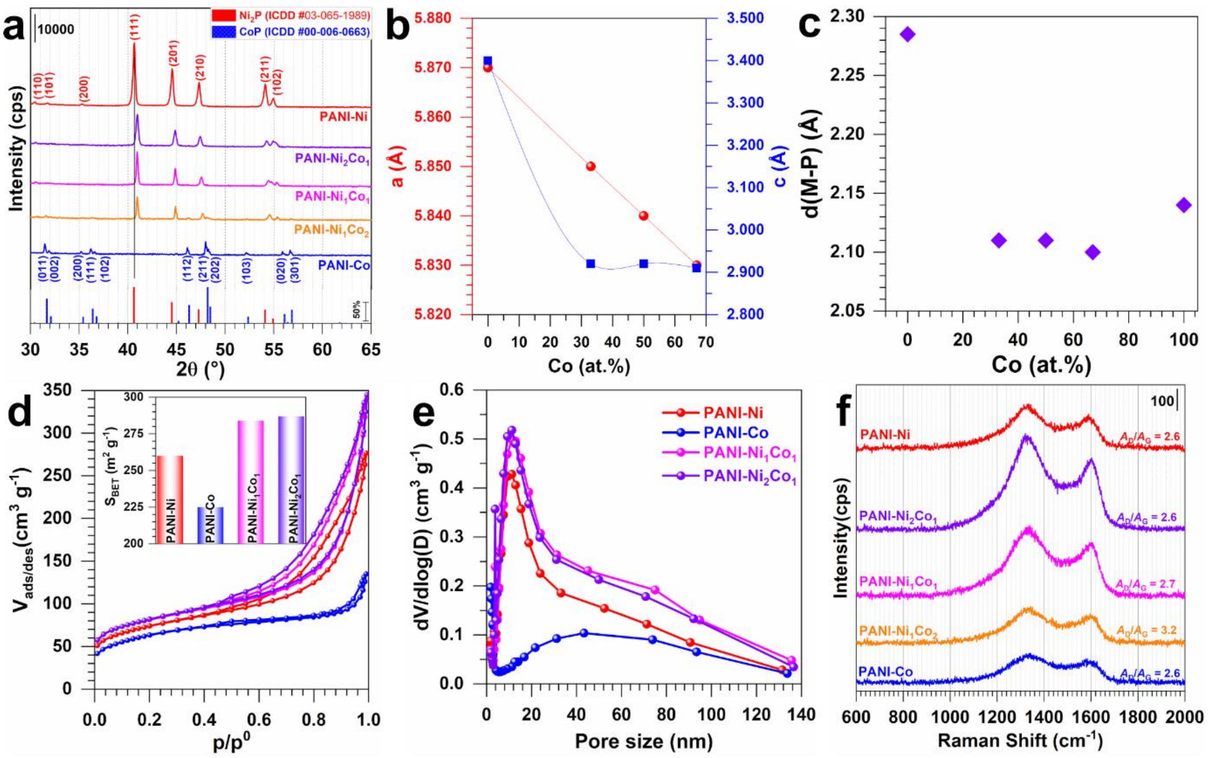

Figure 1. Structural and textural characterization of the materials derived from calcination. a) XRD patterns. b) Variation of the lattice parameters *a* (left *y*-axis, filled circles) and *c* (right *y*-axis, filled squares) for a hexagonal structure as a function of cobalt content (atomic). c) Variation of the Metal-Phosphorus distance *d*(M-P)) for a hexagonal structure as a function of cobalt content (atomic). d) N_2 adsorption-desorption isotherms: inset the BET surface area. e) Pore size (diameter) distribution. f) Raman spectroscopy.

Having demonstrated the ability to synthesize self-supporting monometallic nickel and cobalt phosphide materials, we then synthesized the bimetallic materials designated PANI-Ni_2Co_1, PANI-Ni_1Co_1, and PANI-Ni_1Co_2 by exploring Ni-rich, Co-rich, and equimolar synthesis conditions (Table S1). Prior to the XRD study of the bimetallic phosphide materials named Ni_xCo_yP, we first performed a quantitative elemental analysis by inductively coupled plasma optical emission spectrometry (ICP-OES). The results compiled in Table 1 (data extended in Tables S1 and S2) confirm the Ni/Co atomic ratio of 1.9, 1.0 and 0.5 for PANI-Ni_2Co_1, PANI-Ni_1Co_1, and PANI-Ni_1Co_2, respectively. Interestingly, ICP-OES analysis shows that the (Ni+Co)/P atomic ratio is 1.8, 1.9, 1.8, 1.6 and 1.1 for PANI-Ni, PANI-Ni_2Co_1, PANI-Ni_1Co_1, PANI-Ni_1Co_2 and PANI-Co, which: (i) confirm the XRD results for monometallic phosphides (Ni_2P and CoP), and (ii) suggest that the bimetallic phosphides “NiCoP” may have the structure of Ni_2P, where Co substitutes for Ni, resulting in the structure $Ni_{2-x}Co_xP$ ($0 \leq x < 2$). To probe such a hypothesis, we have performed XRD analysis of bimetallic phosphides. We note that traditional synthesis methods with *ex-situ* phosphidation resulted in a hexagonal structure of “NiCoP”, which was active for electrocatalytic water splitting.[2c,22] We particularly sought to elucidate the crystal structure of the bimetallic phosphide Ni_xCo_yP with respect to the differences between the monometallic phosphides (Ni_2P with a hexagonal structure and CoP with an orthorhombic structure). The diffraction patterns of all bimetallic materials in Figure 1a correspond to a hexagonal crystal structure, that is, a Ni_2P-based phase with partial substitution of Ni atoms by Co atoms[2e] during the carbothermal co-reduction process of the precursors $Ni^{(II)}Cl_2{\cdot}6H_2O$ and $Co^{(II)}Cl_2{\cdot}6H_2O$ in the presence of $H_3P^{(V)}O_4$ and PANI at 900 °C (N_2, 6 h). Indeed, increasing the Co content leads to an upward shift and narrowing of the diffraction peaks in Ni_xCo_yP compared to monometallic Ni_2P due to a distortion of the lattice parameters in the horizontal plane (Figure 1b) and an increase of the crystallite size from 31 to 51 nm (Tables 1 and S2). These changes led to a decrease in the metal-phosphorus distance (d(M-P), M = Ni, Co) (Figure 1c), which can affect the binding energy and electrocatalytic activity of bimetallic materials as a result of a set of three fundamental effects: deformation (long-range geometric lattice deformation), synergistic (multiple metals), and ligand (short-range electronic charge transfer effect).[23] Consequently, Ni_xCo_yP bimetallic phosphides are expected to exhibit improved electrocatalytic performance compared to monometallic phosphides.

Table 1. Physicochemical data extracted from XRD, N_2 adsorption-desorption, Raman spectroscopy, ICP-OES, CHNS-O, EDX and XPS. n.d.: not determined.

Entry		Ni_2P	Ni_2Co_1P	Ni_1Co_1P	Ni_1Co_2P	CoP
XRD	L_v(nm)	32	31	45	51	64
	$d_{(metal\text{-}P)}$(Å)	2.28	2.11	2.11	2.10	2.14
	a(Å)	5.87	5.86	5.84	5.83	-
	c(Å)	3.4	2.92	2.92	2.91	-
	ε(%)a)	-	0.17	0.51	0.68	-
N_2 adsorption-desorption	S_{BET}($m^2\ g^{-1}$)	260	287	284	n.d.	225
	D_{BHJ}(nm)	9.6	10.5	11.2	n.d.	5.7
	V_{total}($cm^3\ g^{-1}$)	0.378	0.482	0.465	n.d.	0.154
Raman spectroscopy	A_D/A_G	2.6	2.6	2.7	3.2	2.6
	L_a(nm)	17.4	17.2	16.8	14	17.3
ICP-OES	Ni+Co(wt%)	50.5	53.7	53.7	52.2	42.7

	Ni+Co+P(wt%)	65.1	68.5	69.2	69.7	63.5
	Ni/Co: atomic	-	1.9	1	0.5	-
	(Ni+Co)/P: atomic	1.8	1.9	1.8	1.6	1.1
EDX	Ni/Co: atomic	-	1.7 ± 0.4	0.9 ± 0.2	0.5 ± 0.1	-
	(Ni+Co)/P: atomic	1.9 ± 0.4	2.2 ± 0.3	2.3 ± 0.6	1.7 ± 0.2	0.9 ± 0.1
CHNS-O	C(wt%)	27.8 ± 0.0	24.7 ± 0.3	23.2 ± 0.1	20.7 ± 0.0	23.5 ± 0.0
	H(wt%)	0.7 ± 0.0	0.7 ± 0.0	0.6 ± 0.0	0.8 ± 0.1	1.1 ± 0.0
	N(wt%)	1.7 ± 0.0	1.4 ± 0.0	1.4 ± 0.0	1.4 ± 0.0	1.5 ± 0.0
	S(wt%)	0.7 ± 0.0	0.8 ± 0.0	0.6 ± 0.0	0.4 ± 0.1	1.0 ± 0.0
	O(wt%)	4.4 ± 0.1	4.1 ± 0.1	5.2 ± 0.1	6.8 ± 0.0	8.7 ± 0.2
	Balanced (wt%)	64.8 ± 0.1	68.3 ± 0.5	68.9 ± 0.1	70.0 ± 0.1	64.2 ± 0.1
XPS	Ni(at%)	1	n.d.	1	n.d.	-
	Co(at%)	-	n.d.	1.8	n.d.	4.2
	P(at%)	2.7	n.d.	3.1	n.d.	4.9
	C(at%)	84.5	n.d.	81.3	n.d.	67.6
	N(at%)	3.2	n.d.	3	n.d.	3.2
	S(at%)	0.8	n.d.	0.8	n.d.	0.9
	O(at%)	7.8	n.d.	9	n.d.	19.2

The N_2 adsorption/desorption analysis (Figure 1d,e) confirms the synthesis of mesoporous materials with a high specific surface area (Brunauer-Emmett-Teller (BET) surface area) of 225-287 $m^2\ g^{-1}$. Pore size distribution profiles (Figure 1e) show heterogeneous pore diameters, suggesting the formation of hierarchical porous structure within the N,S,P-modified carbon networks or the occupation of small pores by Ni_xCo_yP particles, thus exposing large pores. Indeed, bulk CHNS analysis (Tables 1 and S2) revealed C, H, N and S contents of 21-28, 0.7-1.1, 1.4-1.7 and 0.7-1.0 wt%, respectively, depending on the composition of the phosphide materials. In addition, ICP-OES has previously shown that the amount of P varies from 14.6 to 20.8 wt% depending on the composition of the bimetallic phosphides. We then performed Raman spectroscopy to investigate the nature of the carbonaceous species present in/on these carbon-based materials (Figure 1f). The fitted Raman spectra are reported in Figure S1 (the extracted quantitative data are shown in Tables 1 and S2). All materials show two distinct peaks at ca. 1330 and at ca. 1600 cm^{-1}, corresponding to the well-known D-band and G-band of carbon materials, respectively. Two less intense peaks at 1160 and 1480 cm^{-1} are also present and are attributed to sp^3-rich and sp^2-amorphous carbon phases.[24] The ratio of D-band to G-band area, that is, A_D/A_G, which gives the measure of disorder/defects in carbonaceous materials, is summarized in Table 1 and is related to the in-plane crystallite size (L_a). The A_D/A_G (and therefore L_a) values are similar for the different materials (with a slight deviation for PANI-Ni_1Co_2). More specifically, the A_D/A_G (2.6-3.2) and L_a (14.0-17.4 nm) values are within the range of most substrates used in electrocatalysis, such as Vulcan-XC72, CNT, rGO, etc.[4,24-25] (larger than Vulcan-XC72[4a,4c]). Typically, a higher A_D/A_G ratio indicates a greater number of interstitial defects, probably due to the cleavage of C=C bonds leading to the formation of sp^3 hybridized carbon, triggered by the relatively high temperature of the carbothermal co-reduction process. The above results demonstrate the removal of carbon after heat treatment (typical yield after the carbothermal co-reduction process is 15-25%, depending on the chemical composition of the material) and support the hypothesis of metal distribution in the carbon matrix.[26]

Scanning electron microscopy (SEM) and energy dispersive X-ray (EDX) analyses were performed to study the structural morphology and provide detailed information on the spatial distribution of the different structural elements within the Ni_xCo_yP phosphides. SEM images of the control synthesis in the absence of metallic species *versus* the presence of monometallic species are reported in Figure S2. Comparative backscattered SEM of monometallic and bimetallic materials is shown in Figures 2a-e, highlighting the formation of a heterogeneous structure composed of Ni_xCo_yP particles and an N,S,P-modified carbon network, taking into account the elemental mapping (Figures 3 and S3). In Figure 2, there is no obvious predominance of particle morphology as in the previous sulfides[18b] with cone-shaped microscale crystals. Such shapes are governed by the vapor-liquid-solid (VLS) growth mechanism,[27] where the nickel-sulfur vapor creates supersaturation and nucleation at the liquid-solid interface, resulting in axial crystal growth. Furthermore, Figures 2 and S2 shows that the Ni_xCo_yP particles are directly embedded in the carbon network. This ensures a better anchoring of the catalytic particles in the support and therefore a higher stability, as opposed to the conventional case where the metal salt reduction takes place in the presence of a prefabricated support (carbon, metal foam, etc.), resulting only in a surface decoration.[2e,3b,4a] It is even possible that the particles on the surface are covered by a layer of carbon from the carbonaceous atmosphere generated by the decomposition of PANI during the carbothermal reduction process at 900 °C (N_2, 6 h). This will be scrutinized by atomic scale analysis.

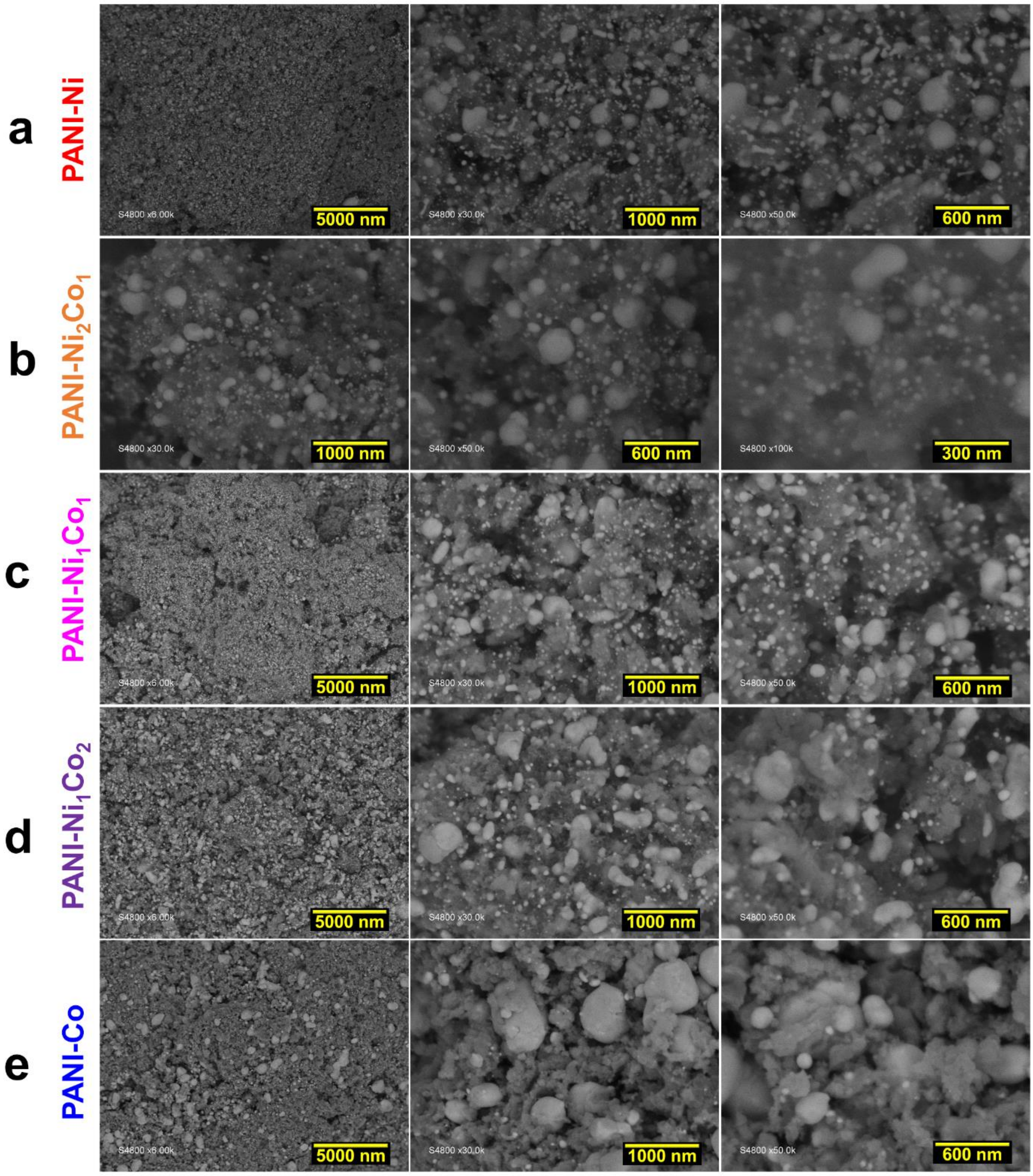

Figure 2. Backscattered SEM images at different magnification (from left to right) for materials derived from: a) PANI-Ni, b) PANI-Ni_2Co_1, c) PANI-Ni_1Co_1, d) PANI-Ni_1Co_2, e) PANI-Co.

Typical EDX spectra and the quantitative data of the different monometallic and bimetallic materials are shown in Figures S4-S5. While the EDX elemental mappings of the monometallic materials (Figure S3) show the coexistence of the metallic species (Ni or Co) and the phosphorus species, Figure 3 clearly shows the overlapping of the Ni, Co and P signals, confirming the formation of Ni_xCo_yP phosphide materials as revealed by the XRD study. The Ni/Co atomic ratios (Table 1) of 1.7 ± 0.4, 0.9 ± 0.2, and 0.5 ± 0.1 for PANI-Ni_2Co_1, PANI-

Ni_1Co_1, and PANI-Ni_1Co_2, respectively, are in agreement with the theoretical expectations and confirm the bulk ICP-OES results. Furthermore, the (Ni+Co)/P atomic ratios (Table 1) of 1.9 ± 0.4, 2.2 ± 0.3, 2.3 ± 0.6, 1.7 ± 0.2, and 0.9 ± 0.1 for PANI-Ni, PANI-Ni_2Co_1, PANI-Ni_1Co_1, PANI-Ni_1Co_2, and PANI-Co, respectively, demonstrate: (i) the formation of Ni_2P structure for PANI-Ni and CoP for PANI-Co, and (ii) the formation of $Ni_{2-x}Co_xP$ ($0 \leq x < 2$) structure.

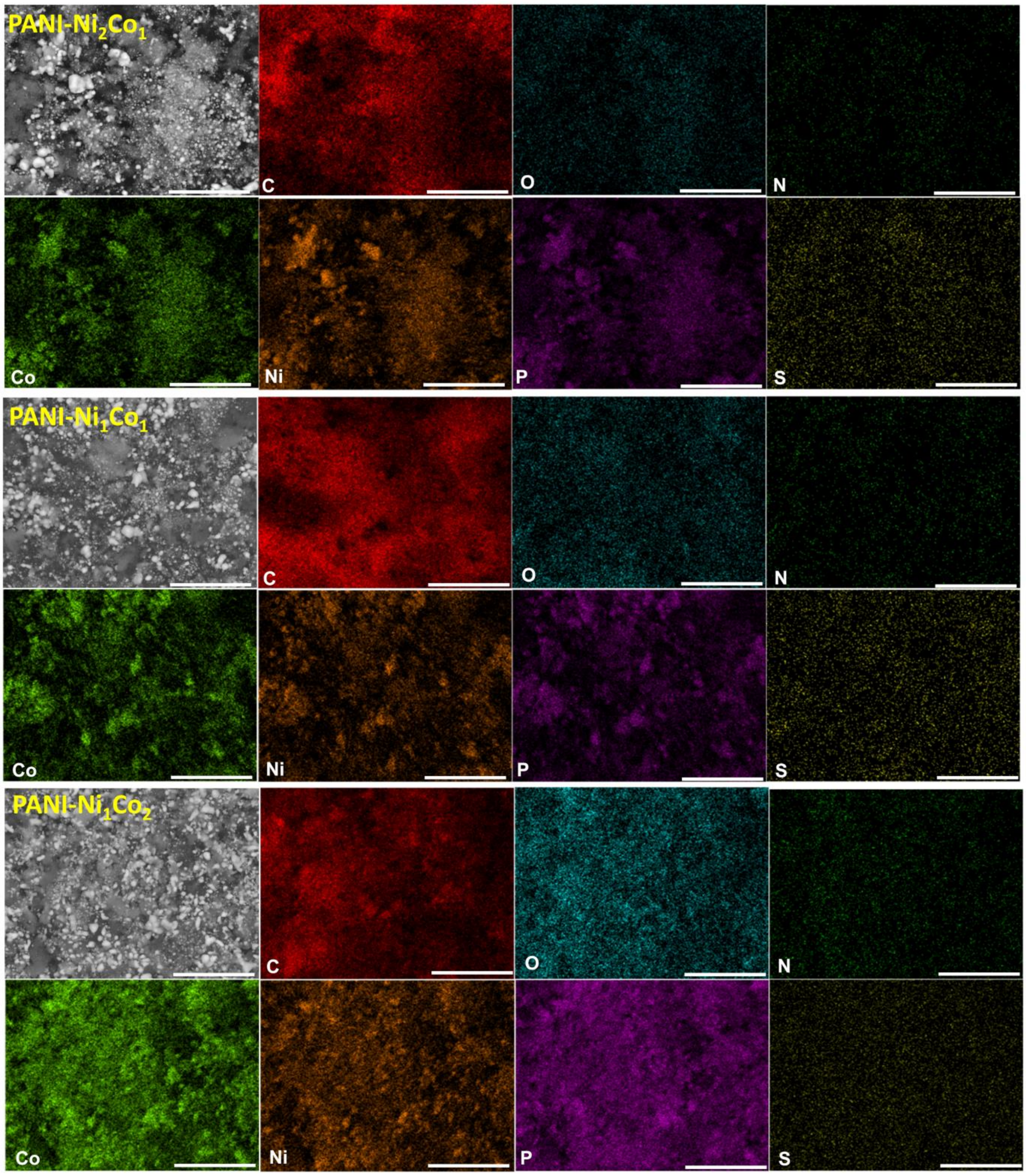

Figure 3. Backscattered SEM images and the corresponding EDX mapping of the bimetallic materials derived from PANI-Ni_xCo_y. Scale bar = 5 µm.

2.1.2. Atomic Scale and Surface Analysis

The above series of bulk and microscopic analyses validate the formation of the Ni_xCo_yP phase within a P,S,N-modified carbon network, thus confirming our initial hypothesis and ruling out the phase segregation despite the discrepancy between the crystal structure of the monometallic phosphides, i.e. Ni_2P (hexagonal) and CoP (orthorhombic). We next sought to carefully determine the detailed atomic arrangement of Ni, Co, and P in Ni_xCo_yP by performing atomic-scale scanning transmission electron microscopy and energy dispersive X-ray spectroscopy (STEM-EDX). Figure 4a-e shows the STEM-EDX elemental mapping and the corresponding EDX line scan intensity profiles. Extended TEM, STEM and EDX results are shown in Figures S6-S17, all confirming the overlap of Ni, Co and P signals, i.e. their coexistence in the same atomic region. In particular, Figure 4a shows the uniform elemental distribution of Ni, Co and P within the PANI-Ni_1Co_1 material at the atomic scale, thus confirming the previous micro-scale SEM-EDX analysis. The EDX line profile of carbon confirms the previous hypothesis that the most exposed Ni_xCo_yP particles on the surface of the N,S,P-modified carbon network are covered by a layer of carbon, which results from the decomposition of polyaniline during the carbothermal reduction process of the metal precursors at 900 °C (N_2, 6 h). For example, in Figure 4a, we would expect to see a clear decrease in the carbon signal on the two Ni_xCo_yP particles, reflecting the difference with the substrate. However, a constant evolution can be seen here, indicating the presence of a carbon layer on the particles (nanoscale layer of carbon whose thickness is difficult to measure precisely).

For monometallic PANI-Ni (Figure S18), the lattice spacing of *d*(hkl) = 0.196 nm corresponds to $2\theta = 46.0°$, which is closed to 47.3°, characteristic of Ni_2P(210), as revealed by the previous XRD study. This result was confirmed by DFT calculations for the surface energy (Table S3), which is 1.55, 1.13, and 0.59 J m^{-2} for the surfaces (111), (201), and (210), respectively. In the case of the bimetallic material PANI-Ni_1Co_1 (Figure S19), the determined value of *d*(hkl) = 0.222 nm corresponds to $2\theta = 40.4°$, which is closed to 40.9° for Ni_2P(111). For the monometallic PANI-Co (Figure S20), the determined value of *d*(hkl) = 0.279 nm corresponds to $2\theta = 32.1°$, close to 31.9° for CoP(011).

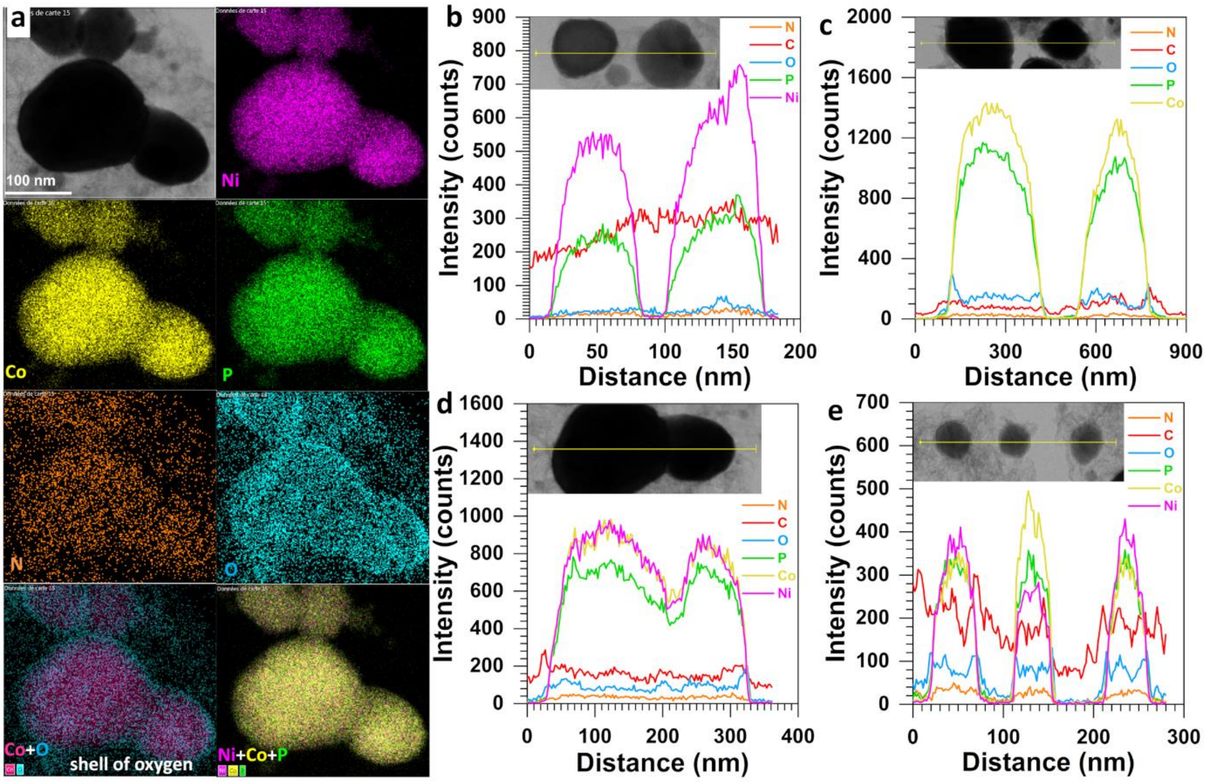

Figure 4. Electron microscopy study. a) STEM-EDX images of the material derived from PANI-Ni_1Co_1 and the corresponding elemental mappings. b-e) EDX line-scan intensity profiles and inset images of the corresponding bright-field STEM images of the materials derived from: b) PANI-Ni (Ni_2P structure), c) PANI-Co (CoP structure), and d-e) PANI-Ni_1Co_1 ($Ni_{2-x}Co_xP$ ($0 \leq x < 2$) structure).

We then used X-ray photoelectron spectroscopy (XPS) to study the surface state and electronic structure of representative materials, i.e., PANI-Ni, PANI-Ni_1Co_1, and PANI-Co. Indexed (low resolution) XPS spectra are shown in Figure S21. Extended quantitative results are shown in Figure S22. This overall analysis shows the presence of Ni, Co, P, C and O elements on the surface of the processed materials (Figure S22), which is in agreement with the SEM-EDX and STEM-EDX analyses. The presence of O is mainly due to air exposure. High-resolution XPS spectra of carbon C 1s (Figure S22a) show the presence of different functional groups C=C (284.6 eV), C-C (285.0 eV) and C-N/C-O/C-S (286.2 eV) derived from polyaniline materials.[18b,28] Similarly, the high resolution N 1s spectra (Figure 5a) are composed of pyridinic-N (398 eV), graphitic-N (400 eV), oxidized-N (403 eV) and oxidized aromatic or π-π* (405, 406 eV).[18b,25] In Figure S22c, the XPS spectra of S 2p can be decomposed into six peaks. The peaks at 161.9 and 162.9 eV are assigned to S $2p_{3/2}$ and S $2p_{1/2}$ of S^{2-}, respectively.[29] Interestingly, these peaks are completely absent in the CoP spectrum, reflecting the weakness of the Co and S interactions. The binding energies at 163.9 and 165.1 eV belong to the thiophene

(C=C-S-C=C) S $2p_{3/2}$ and S $2p_{1/2}$, respectively, while the peaks at 167.9 and 169.1 eV are respectively attributed to surface oxidation of sulfur species upon exposure to ambient air.[30]

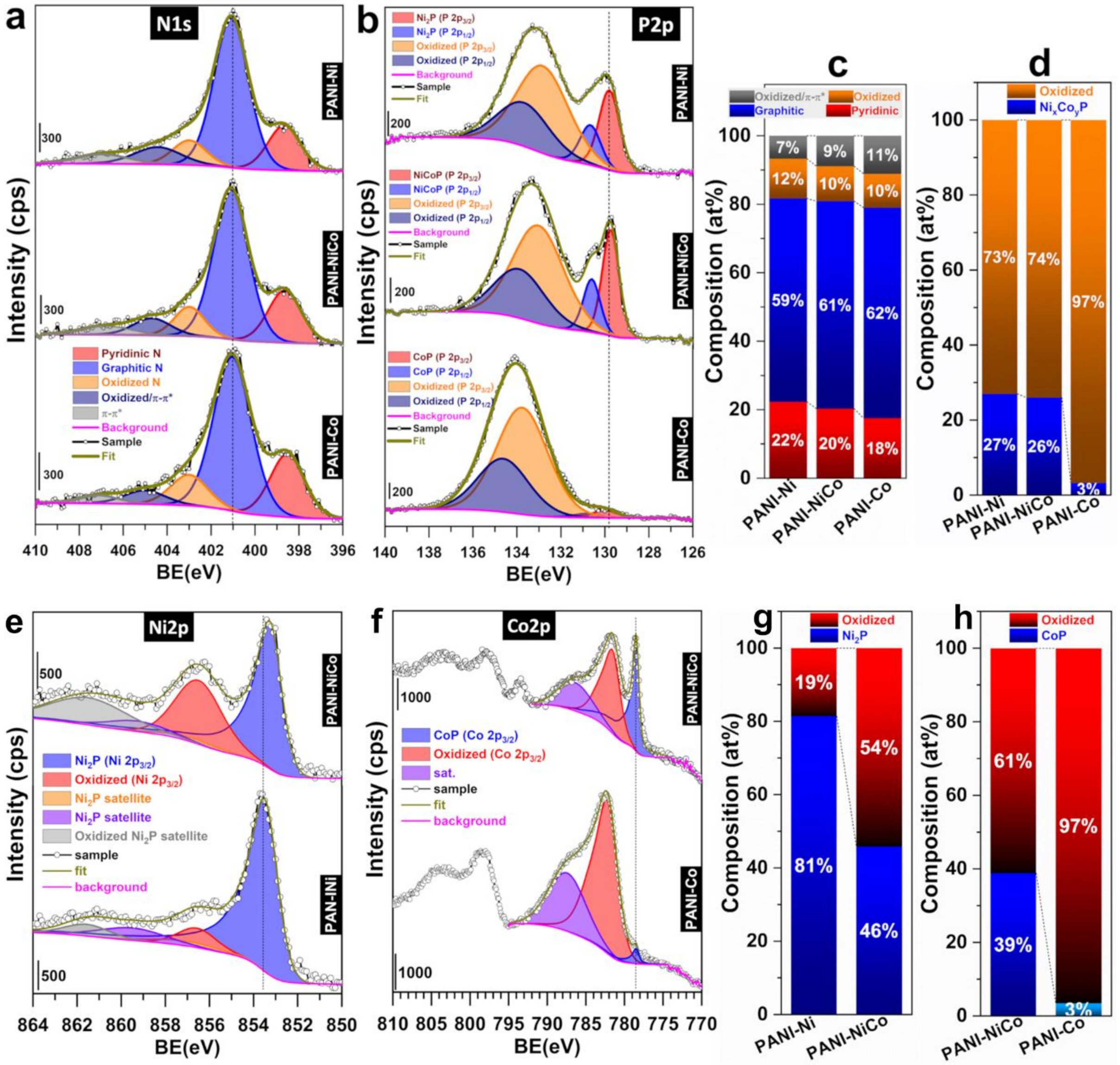

Figure 5. XPS study. High-resolution XPS analysis of: a) N 1s and b) P 2p. Surface atomic composition of: c) N-based species and d) P-based species. High-resolution XPS analysis of: e) Ni 2p and f) Co 2p. Surface atomic composition of: g) Ni-based species and h) Co-based species.

The high-resolution XPS spectra of P 2p can be decomposed into four peaks (Figure 5b). The two spin-orbit splits $2p_{3/2}$ and $2p_{1/2}$ appearing between 129.8-132.8 eV and between 130.7-133.7 eV are assigned to the phosphide and oxidized P species, respectively. For N-based species (Figure 5c), the surface atomic composition is 59-62% graphitic-N, 18-22% pyridinic-N, 10-20% oxidized-N, and 7-11% oxidized aromatic or π-π*. For P-based species (Figure 5d), the surface is mainly composed of oxidized phosphorus species, 26-27 at.% for PANI-Ni and

PANI-Ni_1Co_1, and only 3 at.% is composed of non-oxidized CoP in the monometallic PANI-Co. These results are in agreement with the previous atomic-scale analysis in Figure 5, which already suggests oxygen enrichment of the surface, more pronounced for PANI-Co since cobalt is more sensitive to oxidation than nickel when the materials are exposed to natural atmosphere. We did not detect any bulk oxide materials by high-resolution XRD (Figure 1a). From the high-resolution XPS spectra of Ni 2p for PANI-Ni and PANI-Ni_1Co_1 (Figure 5e), two main peaks with a binding energy of 853.2 and 856.6 eV were assigned to Ni-P and oxidized nickel species, respectively. Satellite peaks with binding energies of 861.6 and 859.9 eV were identified.[31] The high-resolution Co 2p spectra for PANI-Co and PANI-Ni_1Co_1 (Figure 5f) show that the peaks at 778.4 and 781.6 eV belong to Co-P and to the oxidized cobalt species, respectively. The peak located at 786.2 eV is a satellite peak.[32] We note that, in Figure 5f, peaks at binding energies above 795 eV correspond to the spin-orbit split $2p_{1/2}$ of cobalt species already observed at 778.4, 781.6 and 786.2 eV for the spin-orbit split $2p_{3/2}$. The quantitative results of Figure 5g for Ni 2p and Figure 5h for Co 2p suggest that the presence of Co species promotes the oxidation of P within the phosphide structure. The inconsistency between XPS and ICP-OES or EDX regarding the different atomic ratios is due to the relatively large size of the particles, as shown by SEM and S/TEM observations, whilst XPS is limited to a few nanometers. In PANI-Ni_1Co_1, the slight negative shift of the binding energy of P $2p_{3/2}$ suggests that some P atoms can be proton trapping sites, thereby promoting the electrocatalytic hydrogen evolution reaction (HER). Furthermore, it was observed that only the Ni $2p_{3/2}$ peak shifts to a lower binding energy. Thus, the valence state of Ni in PANI-Ni_1Co_1 is more positive than that in Ni_2P, indicating that a partial valence electron transfer occurs between Ni and its surrounding elements (Co, P). On the other hand, the coexistence of Ni, Co and P suppresses the oxidation of P and/or Co, indicating the strong interaction between Ni and Co or P that can protect the surface from extensive oxidation.[33]

2.2. Electrochemical Properties and Electrocatalytic Performance

2.2.1. Electrochemical Characterization and Electrocatalytic Properties

To explore the electrochemical behavior of the synthesized Ni_xCo_yP phosphide materials, cyclic voltammetry (CV) was carried out. Figure 6a depicts the CVs obtained in an alkaline electrolyte. The CV of the PANI-Co material (CoP structure) showed a large redox peak between 1 and 1.3 V vs RHE (reversible hydrogen electrode) attributed to the formation of mixed oxidation states involving the hydroxide species $Co(OH)_2$ and the oxyhydroxide species CoOOH upon polarization, Equations (1-2).[34] During the backwards, the cathodic peak is centered at E_{Co}^{peak} = 1.10 V vs RHE for the inverse electrochemical reaction of Equation (2).

$$Co + 2OH^- \rightarrow Co(OH)_2 + 2e^- \tag{1}$$

$$Co(OH)_2 + OH^- \rightarrow CoOOH + H_2O + e^- \tag{2}$$

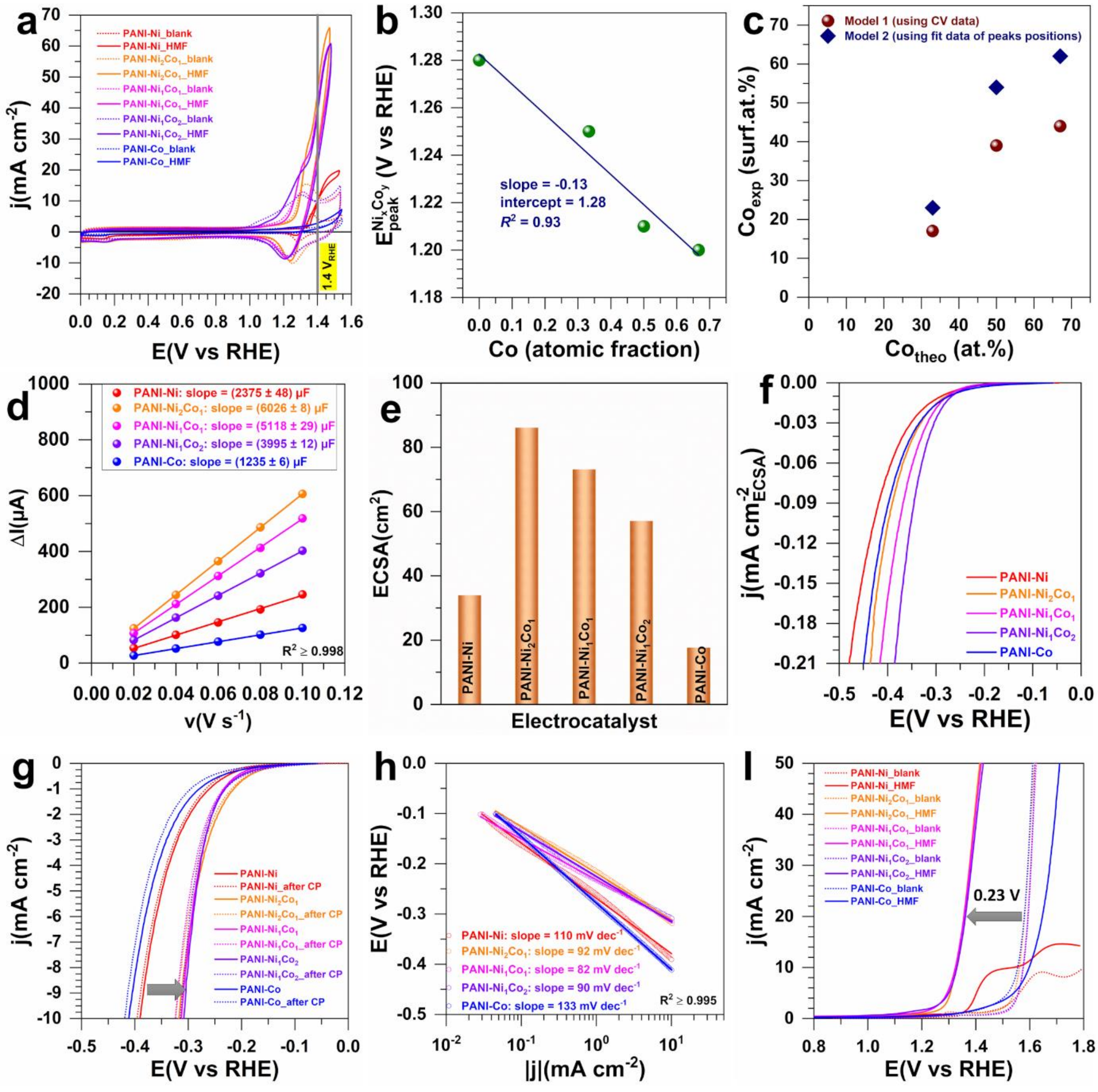

Figure 6. Electrochemistry in 1 M KOH (25 °C, iR-drop uncorrected). a) CVs at 100 mV s^{-1} in the absence (blank) and the presence of 5-HMF (0.1 M). b) Variation of the potential of the main reduction peak from (a). c) Surface atomic composition (from the Rand and Woods method). d) Scan rate dependent absolute value of the double-layer charging current ($\Delta I = I_{anodic} - I_{cathodic}$) at 0.38 V vs RHE for determining ECSA. e) ECSA as a function of the electrocatalyst composition. f) LSV of HER at 5 mV s^{-1}, the current was normalized by ECSA from (e). g)

LSV of HER at 5 mV s^{-1}, the current is normalized by the geometric surface area (0.196 cm^2). h) Tafel plots of HER by the current density from LSV at 5 mV s^{-1}. i) LSV in the absence (blank, OER) and presence of 5-HMF (0.1 M) at 5 mV s^{-1}.

In contrast, the CV of the PANI-Ni material (Ni_2P structure) shows well-defined redox peaks between 1.2 and 1.5 V vs RHE. These peaks are attributed to the presence of nickel hydroxide ($Ni(OH)_2$) and its subsequent oxidation to nickel oxyhydroxide species (NiOOH) according to Equations (3-4).[35] Similarly, during the backwards, the cathodic peak centered at E_{Ni}^{peak} = 1.28 V vs RHE is assigned to the reduction of NiOOH into $Ni(OH)_2$ (inverse electrochemical reaction of Equation (4)).

$$Ni + 2OH^- \rightarrow Ni(OH)_2 + 2e^- \quad (3)$$

$$Ni(OH)_2 + OH^- \rightarrow NiOOH + H_2O + e^- \quad (4)$$

For the bimetallic-based electrode materials, Ni_xCo_yP, the observed reduction peak for all synthesized nanostructured materials corresponds to the reduction peak of the oxyhydroxide species $Ni_{1-x}Co_xOOH$. It is sharper and broader than that of Ni_2P due to the modification of the surface structure by cobalt species. This observation confirms the results obtained by XRD. The surface atomic composition of Ni_xCo_yP alloys was determined by the electrochemical method proposed by Rand and Woods and described by Equations (5-6).[36]

$$E_{NiCo}^{peak} = \chi_{Ni} E_{Ni}^{peak} + \chi_{Co} E_{Co}^{peak} \quad (5)$$

$$\chi_{Ni} + \chi_{Co} = 1 \Rightarrow \chi_{Ni} = \frac{E_{NiCo}^{peak} - E_{Co}^{peak}}{E_{Ni}^{peak} - E_{Co}^{peak}} \quad (6)$$

Where χ_{Ni} and χ_{Co}($\chi_{Ni} = 1-\chi_{Co}$) are the Ni and Co surface atomic fractions E_{Ni}^{peak}, E_{Co}^{peak} and E_{NiCo}^{peak} are the oxide reduction peak potentials for Ni, Co and NiCo, respectively.

Since the observed reduction peak corresponds to the reduction of $Ni_{1-x}Co_xOOH$ species formed on the catalyst surface during anodic scan, the potential of the reduction peak reflects the composition of the catalyst surface and can therefore be used to determine the composition of the surface alloy present in Ni_xCo_yP, as proposed by Rand and Woods.[36] In Figure 6a, the alloyed phosphide materials have a reduction peak shifted away from the monometallic at 1.25, 1.21 and 1.19 V vs RHE for PANI-Ni_2Co_1, PANI-Ni_1Co_1, PANI-Ni_1Co_2, respectively (at 1.28 and 1.10 for PANI-Ni and PANI-Co, respectively). Figure 6b highlights the validation of the

Rand and Woods model described by Equations (5).[36] Since the cathodic peak associated with the $CoOOH/Co(OH)_2$ redox couple is broad with an estimated position of $E_{Co}^{peak(Model\ 1)} = 1.10$ V vs RHE, the fit of Figure 6b leads to a value of $E_{Co}^{peak(Model\ 2)} = 1.15$ V vs RHE for $CoOOH/Co(OH)_2$. These two values were used in Equation (6) to derive the surface atomic compositions shown in Figure 6c. The first model gives low values of the atomic surface composition with respect to the theoretical composition (confirmed by ICP-OES elemental analysis), which could be explained by surface nickel enrichment during voltammetric cycles, a phenomenon well known in electrochemistry.[37] The second model gives values of the atomic surface composition close to the theoretical values, suggesting preservation of the microstructure, which is more likely given the uncertainty in the precise determination of E_{Co}^{peak} by CV.

Since the redox peaks associated with cobalt species are not well defined, we next estimated the electrochemically active surface area (ECSA) by the double layer charging current method from CVs in the non-faradaic region (0.330-0.427 V vs RHE) at different scan rates (100-20 mV s^{-1}). The CVs profiles are reported in Figure S23, while the electrochemical double-layer capacitance (C_{dl}) from the slope of the scan rate dependent absolute value of the double-layer charging current ($\Delta I = I_{anodic} - I_{cathodic}$) at 0.38 V vs RHE is shown in Figure 6d. The determined C_{dl} values are 2375 ± 48, 6026 ± 8, 5118 ± 29, 3995 ± 12, and 1235± 6 µF for PANI-Ni, PANI-Ni_2Co_1, PANI-Ni_1Co_1, PANI-Ni_1Co_2, and PANI-Co, respectively. Using the average specific capacitance, C_s of 2×35 µF cm^{-2} (although there is no standard value for the specific capacitance, which can vary from 11 to 130 µF cm^{-2}),[38] the ECSA (= C_{dl}/C_s) varied from 34 for PANI-Ni (18 for PANI-Co) to 57-86 cm^2 for the bimetallic materials (Figure 5e), highlighting a 2-3-fold increase in the potential surface area accessible to electrocatalysis. The trend in ECSA is similar for the previous BET surface area (Figure 1d). It is worth mentioning that ECSA using the capacitive double-layer method refers to the surface area accessible to the electrolyte solution, unlike BET surface area, which represents the surface area of all materials available for physical adsorption of N_2 gas. Likewise, in contrast to some widespread misconceptions, the number of ECSA-derived active sites determined in the non-faradaic region is likely to differ from the sites that will be engaged during the faradaic reactions, since the adsorption sites of the reactions/intermediates may be different.

Next, we aimed to evaluate the electrocatalytic performance of the synthesized materials for hydrogen generation by using the synthesized phosphide Ni_xCo_yP as bifunctional electrode materials for both HER and 5-HMF oxidation (as an alternative to OER[1c,13-14]). In the presence of 5-HMF, the oxidative peaks of $Ni(OH)_2$ disappeared reflecting the activity of the synthesized materials for 5-HMF electrooxidation (Figure 6a), which is in agreement with other previous works.[39] The electrocatalytic activity of Ni_xCo_yP electrodes for HER is reported in: (i) Figure 6f when the current from the linear sweep voltammetry (LSV) is normalized by ECSA from Figure 6e, and (ii) Figure 6g when the LSV current is normalized by the geometric surface area. The comparison of the HER performance of the prepared electrocatalysts with previously reported phosphide-based electrocatalysts is reported in Table S4. Figure 6f shows that the bimetallic electrocatalysts have a much higher activity per active site, which is consistent with the previous physicochemical and electrochemical characterization. The overpotential required to reach the metric current density of $|j| = 10$ mA cm^{-2} is 322, 317, 336, 299 and 411 mV, for PANI-Ni, PANI-Ni_2Co_1, PANI-Ni_1Co_1, PANI-Ni_1Co_2, and PANI-Co, respectively. The same trend was also obtained even after chronopotentiometry test at $j = -10$ mA cm^{-2} (Figure S24). Mechanistically, HER can occur *via* three elementary steps as mentioned below (Equations (7-9) with the corresponding Tafel slope (b), where H_{ads} represents the H atom adsorbed on the active site “*” (α: symmetry coefficient, F: Faraday constant, R: ideal gas constant, T: absolute temperature).

$$H_2O + * + e^- \rightarrow *\text{-}H_{ads} + OH^-, \quad \text{Volmer step,} \quad \left(b = \frac{2.3RT}{\alpha F} = 118 \text{ mV dec}^{-1} \text{ at } 25\ °\text{C}\right) \quad (7)$$

$$*\text{-}H_{ads} + *\text{-}H_{ads} \rightarrow H_2 + 2*, \quad \text{Tafel step,} \quad \left(b = \frac{2.3RT}{2F} = 29 \text{ mV dec}^{-1} \text{ at } 25\ °\text{C}\right) \quad (8)$$

$$*\text{-}H_{ads} + e^- + H_2O \rightarrow H_2 + OH^- + *, \quad \text{Heyrovsky step,} \quad \left(b = \frac{2.3RT}{(1+\alpha)F} = 39 \text{ mV dec}^{-1}\right) \quad (9)$$

From Figure 6h, the HER Tafel slope values indicate that the Volmer reaction is the limiting step, that is, the dehydrogenating adsorption of water molecules on the electrocatalytic surface.[40] Indeed, experimentally observed Tafel slopes of 80-130 mV dec^{-1} correspond to a symmetry coefficient of $\alpha = 0.72\text{-}0.45$ in Equation (7), suggesting that there are mass transfer issues that merge with the electrons transfer kinetics of the Volmer step.[41] The coexistence of Ni, Co and P in the same material allows to maximize the three fundamental effects, namely, the deformation (long-range geometric lattice deformation), synergistic (multiple metals), and ligand (short-range electronic charge transfer effect).[23] The enhanced catalytic activity of the synthesized electrode materials towards HER can also be explained by the formation of bipolar $M^{\delta+}\text{-}P^{\delta-}$ (M = Ni, Co), where the proton acceptor ability is promoted, which favors the water dissociation. Finally, the presence of both Ni and Co leads to a synergistic effect where protons are known to bind strongly to the Ni surface while they bind weakly to Co, leading to an antagonistic behavior towards H adsorption/desorption, which is favorable to enhance HER.[42]

In fact, experimental data show that the key step is the Volmer reaction (H_2O + * + e^- → *-H_{ads} + OH^-, where "*" is the active site and H_{ads} is the H atom adsorbed on the active site) on the Ni_xCo_yP electrocatalyst. Therefore, it is hypothesized that when a molecule of H_2O approaches the Ni_xCo_yP electrocatalytic surface, electron density transfer from partially and positively charged $M^{\delta+}$ metal centers (M = Ni and Co) to partially and negatively charged phosphorus atoms ($P^{\delta-}$), as well as pendant phosphorus and oxygen atoms, contributes to the weakening of the H–OH bond.[42a,42c,42d] This hypothesis concurs with the XRD, XPS and CV analyses mentioned above, which showed, for Ni_xCo_yP, distortion of lattice parameters, variation in metal-phosphorus atomic distance, shifting of binding energies and displacement of the oxides reduction peak. Thus, upon cleavage of these H-OH bonds, the hydroxyl species are preferentially adsorbed onto Ni-based active sites, while the proton species are transferred to adjacent cobalt and phosphorus active sites. Consequently, Ni- and Co-based active sites are involved in both Volmer (Equation (7)) and Heyrovsky (Equation (9)) steps, while Co- and P-based active sites are involved in Tafel steps (Equation (8)). It is known that this key role of Co helps to stabilize the neighboring active sites of other metals such as Ni, Mo, etc.[43] Finally, the overall electrocatalytic performance of the synthesized phosphide-based bimetallic electrocatalyst, Ni_xCo_yP, is determined by the delicate balance of electrocatalytic activity of the two metal species, i.e. desorption of hydroxyls from Ni-based active sites and desorption of H_{ads} from Co-based active sites.

To investigate the electrocatalytic activity of the synthesized electrode materials for the 5-HMF electrooxidation, the electrocatalytic OER activity in the absence of 5-HMF was also studied to account for the postulated reduction in the anode overpotential of an electrolysis cell for H_2 production when OER is replaced by the electrooxidation of 5-HMF.[1c,44] Figure 6i shows the polarization curves recorded on different Ni_xCo_yP electrode materials, which confirm a decrease of around 0.23 V in the anode potential, hence a significant lowering of the cell voltage of a potential H_2-production electrolyzer since $U_{\mathrm{cell}} = E_{(+)} - E_{(-)} = E_{(\mathrm{anode})} - E_{(\mathrm{cathode})}$. Tables S5 (OER) and S6 (5-HMF) summarize the comparison with the literature. The presence of 5-HMF increases the current density in the potential range of 1.2-1.4 V vs RHE. For the bimetallic electrocatalysts, the onset potential for 5-HMF electrooxidation is significantly shifted to lower potentials as well as the potential required to achieve a current density of 10-50 mA cm^{-2}. These observations clearly show that the design of a bimetallic phosphide material Ni_xCo_yP plays a crucial role in improving the electrocatalytic activity. Previous DFT studies through the density of state (DOS) indicate that the *d*-band for Co-Ni-P is closer to the Fermi level, which suggests a better performance and a lower intermediate adsorption energy.[45]

2.2.2. Bulk Electrolysis

We next interrogated the selective conversion of HMF to FDCA under constant potential, choosing 1.42 V vs RHE based on the previous dynamic studies by CV (Figure 6a) and LSV (Figure 6i). High performance liquid chromatography (HPLC) analysis was performed on the course of electrolysis. To find the best conditions for HPLC analysis, we first recorded the UV-visible spectra of 5-HMF and the electrooxidation reaction by-products (based on Scheme 1) in the full range from 200 to 800 nm (Figure S25), leveraging on the seminal procedure developed by Kokoh and his colleagues for the selective electrooxidation of 2,5-dihydroxymethylfuran in alkaline media.[46] We have observed that the appropriate choice of wavelength when quantifying the 5-HMF reaction and its oxidation products by HPLC with UV-vis detection is $\lambda = 265$ nm. We note that $\lambda = 265$ nm coincides with the maximum absorption wavelength of FDCA.[47] FDCA production, total charge and faradaic efficiency of 5-HMF electrolysis are shown in Figure 7a-d. It is evident that the concentration of 5-HMF decreases along the electrolysis process while the concentration of FDCA product increases. The highest total charge and FDCA concentration were obtained with PANI-Ni_1Co_1. The continuous increase in FDCA concentration throughout the electrolysis for PANI-Ni_2Co_1 and PANI-Ni_1Co_1 materials (Figure 7c) confirms their high electrocatalytic activity, in agreement with previous CV studies. The persistence of FDCA production throughout the experiment suggests that these catalysts effectively maintain accessible active sites for the adsorption and conversion of 5-HMF, demonstrating efficient catalytic stability and activity (Figure 7a). HPLC chromatograms confirm the production of the intermediate HMFCA and FDCA (Figure 7b). In particular, PANI-Ni_1Co_1 and PANI-Ni_2Co_1 produced higher FDCA peaks, reflecting the higher current densities and electrical charges observed above. This suggests a higher catalytic turnover for these bimetallic systems. In contrast, PANI-Ni and PANI-CoP showed a reduced FDCA peak intensity, indicating lower conversion, probably due to suboptimal adsorption of 5-HMF and slower oxidation kinetics. It should be noted that 2,5-furandicarbaldehyde (FDA) was not observed in the overall reaction, probably because the oxidation of the aldehyde group was more favorable than that of the HMF alcohol group in our system or because of the low chemical stability of an aldehyde group undergoing the Cannizzaro reaction in alkaline media.[47a,48]

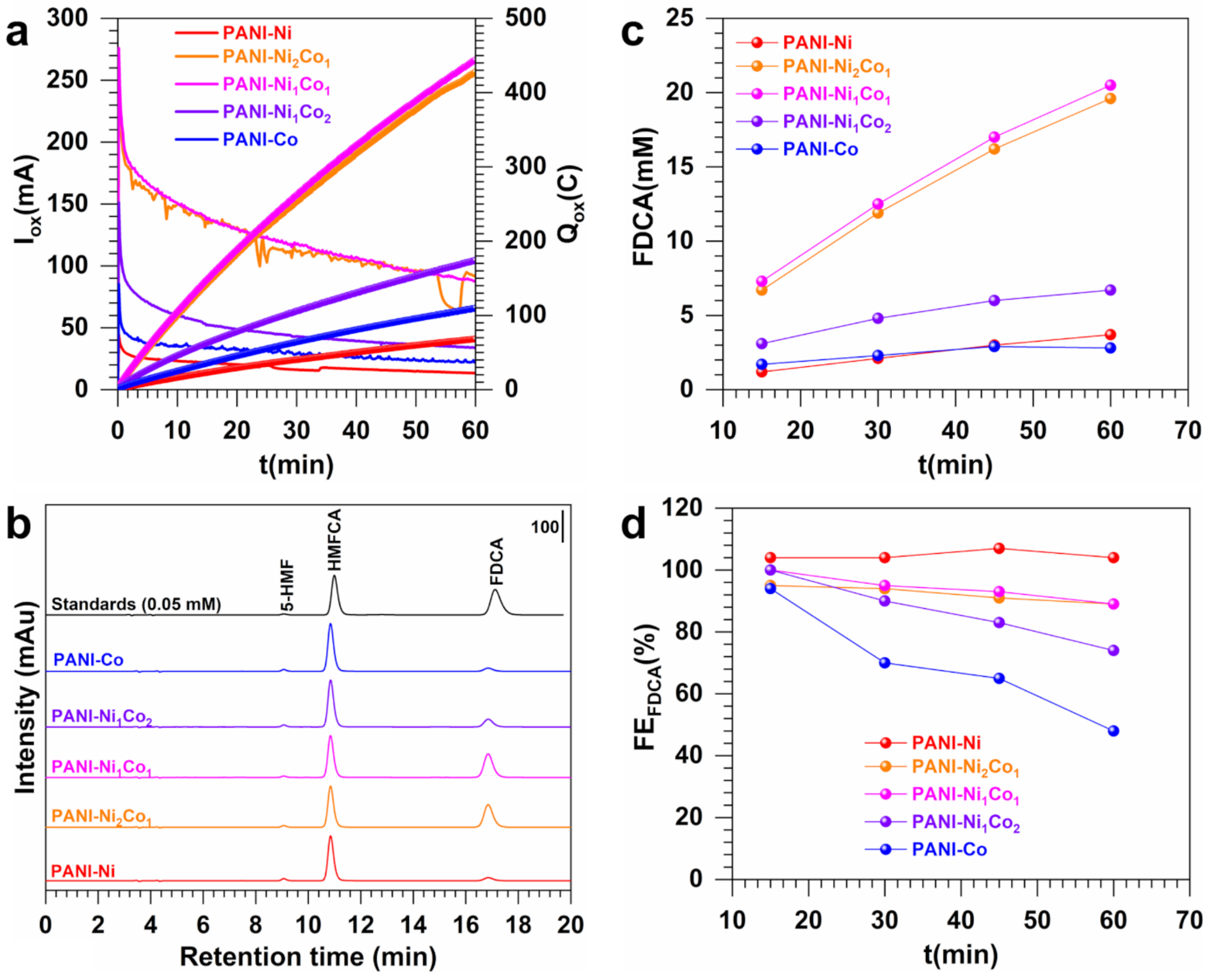

Figure 7. Bulk electrolysis (electrolyte: KOH (1 M); substrate: 5-HMF (0.1 M); temperature: 25 °C; working electrode: GDE (20 mm high, 25 mm width, 370 µm thickness)). (a) Current and electrical charge during the electrolysis. (b) Chromatograms from HPLC (Eluent: 0.6 mL min^{-1} of H_2SO_4 (pH 2.19, 900 mL) + MeOH (50 mL) + MeCN (50 mL); injection: 20 µL; column: Atlantis dC18 Column, 5 µm, 4.6×150 mm (20 °C)) of the standards and electrolysis products (diluted 500 times before analysis). (c) Concentration of FDCA product during the electrolysis. (d) Faradaic efficiency for HMF-to-FDCA electroconversion.

The trends observed in the faradic efficiency during the bulk electrolysis of 5-HMF in FDCA (Figure 7d) highlight significant differences between the catalysts, particularly related to the presence and the content of nickel. PANI-Ni, PANI-Ni$_2$Co$_1$ and PANI-Ni$_1$Co$_1$ maintained high and stable faradic efficiencies (>99%) throughout the electrolysis process, while PANI-Ni$_1$Co$_2$ and PANI-Co showed a significant decrease in FDCA faradic efficiency over time. These results reflect the high selectivity of bimetallic electrodes when the nickel content is at least 50 at.%, with PANI-Ni$_2$Co$_1$ and PANI-Ni$_1$Co$_1$ providing efficient electron transfer for 5-HMF oxidation, leading to high productivity (high current density (Figure 7a) and higher FDCA concentration (Figure 7c)) and faradic efficiency (Figure 7d). On the other hand, decreasing yields were observed in the cases of PANI-Ni_1Co_2 and PANI-Co, where the Co content is higher than that of Ni. This suggests that the selectivity of CoP towards FDCA formation is lower than that of Ni_2P. This allows us to postulate that an excess of cobalt may not support the oxidation pathway as effectively, presumably because of less favorable interactions with the reactants or facilitation of side reactions that consume electrons without producing FDCA. The specific Ni/Co ratio therefore appears to be critical, as the right balance can significantly influence the electrocatalytic process by maintaining an environment conducive to efficient electron utilization and catalytic stability. For example, monometallic PANI-Ni leads to the highest faradaic efficiency, but the current density is significantly low when considering the LSV (Figure 6i) and chronoamperometry (Figure 7a) results. In conclusion, the best compromise in terms of current density and faradaic efficiency is $Ni_{2-x}Co_xP$ when $0.5 \leq x \leq 1$.

2.2.3. Spectroelectrochemistry

To better understand the mechanism of 5-HMF electrooxidation, *in situ* infrared spectroscopy is performed during dynamic voltammetry (CV) and potentiostatic (chronoamperometry) tests, known as spectroelectrochemistry. Figure S26 shows the reference FTIR spectra of 5-HMF and FDCA, and the corresponding infrared specific bands are listed in Table S7. Figure 8a-d and Figure S27-S29 show single-potential infrared alteration spectra (SPAIRS or CV-FTIRS) recorded during 5-HMF electrooxidation for synthesized electrode materials by recording the electrode reflectivity at different potentials (step = 0.05 V) at the quasi-steady state scan rate of 1 mV s^{-1}. The CA-FTIRS coupling by recording a spectrum every $\Delta t = 3$ min with the electrode potential poised at 1.42 V vs RHE is shown in Figure 8e-f and Figures S30-S33. We selected a value of 1.42 V vs RHE for comparison with previous studies using electrolysis and HPLC. Oxidation of 5-HMF results in the appearance of three bands in the 1100-1600 cm^{-1} region, regardless of the method, so the reaction products are the same. We note that the same bands are observed during the forward scan (Figure 8a) and the reverse scan (Figure 8b), meaning that the nature of the reaction products is similar during the CV in Figure 8c, which has been previously reported for glucose electrooxidation.[49] Specifically, the bands at about 1400 and 1600 cm^{-1} are assigned to (O-C-O) asymmetric stretching and to (O-C-O) symmetric stretching, respectively, resulting from the formation of FDCA. The band observed at about 1200 cm^{-1} is characteristic of the C-C bond, which is considered unbroken during the electro-oxidation of 5-HMF.[11b,44b,50] Another important result is that the bands of FDCA formation appeared at different potentials depending on the electrode materials. They appear at 1.47 V vs RHE on monometallic electrocatalysts and at about 1.02 V vs RHE on bimetallic materials. These results can explain the slow kinetics of 5-HMF electrooxidation on Ni_2P and CoP electrode materials and thus their low faradic efficiency. So far, it is clear that the main reaction product is FDCA, as evidenced by HPLC analysis. The upward bands at 1900 and 2600 cm^{-1} can be assigned to the carbonyl and hydroxyl consumption, characteristic of 5-HMF electrooxidation. Furthermore, the *in-situ* FTIRS study coupled with chronoamperometry at 1.42 V vs RHE shows that the intensity of the bands characteristic of the FDCA product increases during the course of the reaction, which is consistent with the increase in concentration during bulk electrolysis and HPLC studies at the same electrode potential.

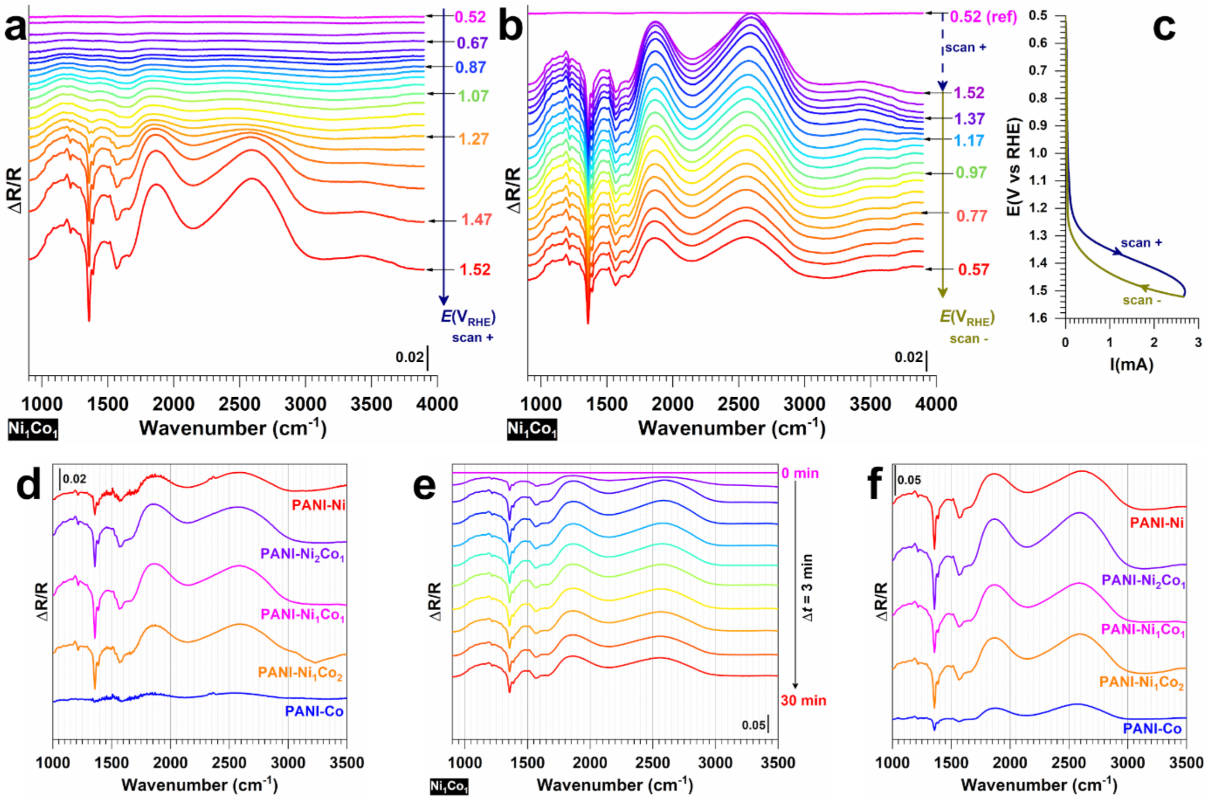

Figure 8. Spectroelectrochemistry in KOH (1 M) + 5-HMF (0.1 M). (a-c) SPAIRS (reference potential = OCP = 0.52 vs RHE) on PANI-Ni_1Co_1 at a quasi-steady state scan rate of 1 mV s^{-1}, spectra recorded every ΔE = 50 mV for: (a) Positive (forward) scan, (b) Negative (backward) scan, and (c) Corresponding CV (iR-drop uncorrected). (d) Compared SPAIRS results at 1.42 V vs RHE during the forward-going scan. (e) *In situ* FTIR spectra during CA at 1.42 V vs RHE on PANI-Ni_1Co_1. (f) Compared spectra at t = 9 min at a poised CA potential of 1.42 V vs RHE. Temperature: 22 ± 2 °C

2.3. Computational Study

To elucidate the reaction mechanisms involved in the deprotonation of 5-HMF on the Ni_2P-based catalytic surface, DFT calculations were performed. Figure 9 illustrates several potential intermediates along deprotonation pathways A and B (see Scheme 1). Initially, the gas-phase 5-HMF molecule (Figure 9a) undergoes exothermic molecular adsorption (Figure 9b). Surface interactions involving both the aldehyde and alcohol groups (configuration H1) or solely the aldehyde group (configuration H2) exhibit competitive computed adsorption energies of -1.02 and -1.00 eV, respectively. DFT optimizations of various structures resulting from the initial protonation of adsorbed 5-HMF (see Figure 9c) indicate the superior stability of intermediates derived from pathway B (B1 and B2). These two intermediates (+0.00 eV and +0.03 eV) are equivalent and arise from the O-H bond breaking in the aldehyde group. Importantly, the calculated intermediate resulting from deprotonation of the C-H bond in the aldehyde group is predicted to be highly endothermic (B3 = +0.6 eV). Similarly, intermediates resulting from pathway A, where the initial deprotonation may occur subsequent to the breaking of the C-H bond in the alcohol group (A1 and A2), are found to be less favorable by +0.2 and +0.1 eV, respectively. These DFT results align with experimental observations, and further investigations into transition states and the influence of applied potential will be pursued in future studies. Indeed, it is well known that the reaction pathway depends strongly on the pH of the medium. Under strong alkaline media ($pH \geq 13$) path B is favored over path A. However, ex situ techniques (HPLC) cannot absolutely determine the mechanism pathway of the reaction. Even if only FDCA and HMFCA are detected by HPLC, their presence of the first pathway B's product FDA cannot be completely excluded given it possible decomposition in alkaline media by Cannizzaro's reaction.[47a,48] Conclusively, the oxidation of 5-HMF to FDCA involves the oxidation of both alcohol and aldehyde functional groups.

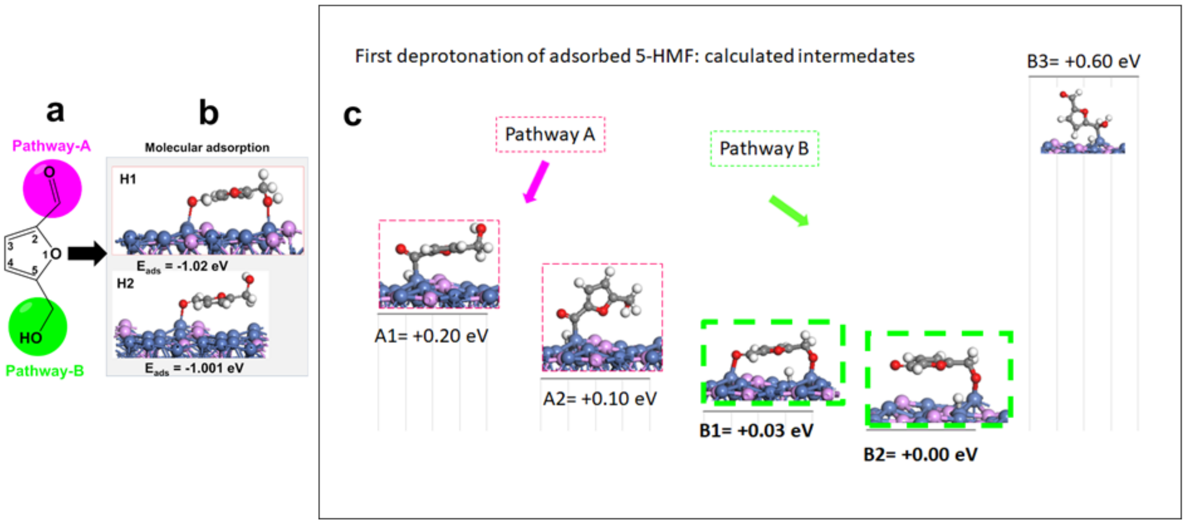

Figure 9. DFT calculations of the adsorption of the 5-HMF (5-Hydroxymethylfurfural) molecule on a Ni_2P (111) surface and subsequent deprotonated intermediates. a) Molecule of 5-HMF. b) Molecular adsorption of 5-HMF without deprotonation. c) In purple, deprotonated intermediates (A1 and A2) resulted from the pathway-A: deprotonation via C–H breaking of alcohol group. In green, deprotonated intermediates resulted from pathway B: via O-H breaking (B1, B2) and via C-H breaking (B3) of aldehyde group. The energy reference is calculated with respect to the most stable total energy intermediate (B2) in eV.

2.4. Long-Term Electrolysis and HMF Electrooxidation Pathways

We also designed a specific bulk electrolysis setup to study the behavior of the anode (E_A) and cathode (E_C) potentials during a galvanostatic operation to find the limiting electrode by inserting a tiny reference electrode (RHE, MiniHydroFlex®, Bio-Logic) in each compartment. Figure 10a (the detailed experimental setup is shown in Figure S36) shows the developed temperature-controlled H-type cell using a Sustainion® X37-50 Grade RT membrane as the hydroxide AEM separating the anode compartment [KOH (1 M) + 5-HMF (0.1 M)] from the cathode compartment [KOH (1 M)]. Note that the orange color is characteristic of an aqueous 5-HMF solution. We started applying the current between the anode and the cathode 2 minutes after the start of the OCP measurement (see Figure S36) to verify that the measurement of EC is correct. Figure 10b shows the E_A and E_C profiles for an applied current of $I_{applied}$ = 20 mA [catalytic ink loaded onto both sides of GDE (10 mm high, 10 mm width, 370 µm thickness)] to avoid complete and rapid oxidation of 5-HMF. The results for the first hour are shown in Figure S37. Here, the 13.36 hours tested are shorter than the 36 hours required for complete conversion of HMF to FDCA, assuming 100% faradic efficiency for the 6 electrons transferred, Equation (10). Despite these considerations, the significant increase in the anode potential after

4 h of electrolysis, from about 1.2 V vs RHE at the beginning to 1.6 V vs RHE at the end, is due to the consumption of 5-HMF in the vicinity of the electrode, as well as a possible accumulation of reaction products and the availability of active sites. In fact, as discussed below, for the most likely mechanism of indirect 5-HMF oxidation, the applied current at the anode is used to electrooxidize the metal and hydroxyl species to oxyhydroxide species, whose reduction back to hydroxyl species releases electrons to oxidize 5-HMF.[44a,51] For the cathode, the potential does not change significantly. Note that both electrode potentials fall within the range of the half-cell study (Figure 6a and 6g). Detailed post-mortem SEM and EDX analyses of the anode and cathode electrodes are shown in Figure 10c for the anode and Figure 10b for the cathode (high-resolution backscattered SEM and EDX quantification are shown in Figures S38-S39). Overall, with the Ni/Co atomic ratios being 0.9 ± 0.1 for the cathode ((Ni+Co)/P atomic ratio 3.3 ± 0.7) and 0.9 ± 0.2 for the anode ((Ni+Co)/P atomic ratio 3.0 ± 0.4), there is a light decrease of P content (the studied material was PANI-Ni_1Co_1 (initial atomic ratios of Ni/Co = 0.9 ± 0.2 and (Ni+Co)/P = 2.2 ± 0. 3).

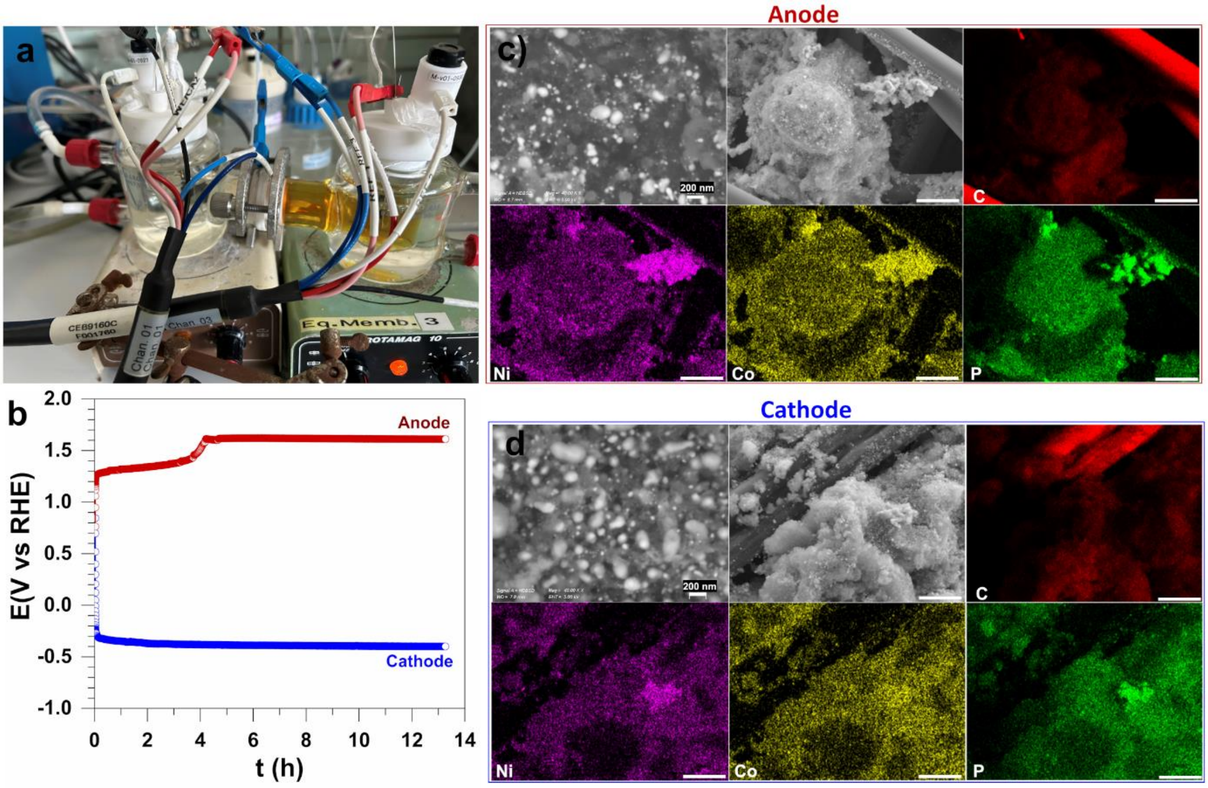

Figure 10. Long-term stability test and post-mortem analysis. (a) Photograph of the homemade temperature-controlled and compartmentalized H-type cell [temperature of 25 °C, Sustainion® X37-50 Grade RT hydroxide AEM separated the anode compartment (KOH (1 M) + 5-HMF (0.1 M), 45 mL) to that of the cathode compartment [KOH (1 M), 35 mL]; each compartment

has a reference electrode (RHE, MiniHydroFlex®). b) Potentials of the anode and the cathode recorded during the galvanostatic operation at an applied current I_{applied} of 20 mA (corresponding to a current density j_{applied} of 10 mA cm^{-2}). (a) Potential-time trace of the cathode (HER). (b) Potential-time trace of the anode (5-HMF electrooxidation). Post-mortem backscattered SEM images and the corresponding EDX mapping for the electrodes after prolonged electrolysis (panel (b)): c) Anode, and d) Cathode. The tested electrocatalyst was Ni_1Co_1P. Scale bar = 10 µm.

Finally, based on the HPLC and spectroelectrochemical analysis, it is possible to propose a scheme of the reaction mechanism of 5-HMF electrooxidation on the synthesized Ni_xCo_yP electrode materials (Scheme 3). It is known that in alkaline medium and in the presence of electrocatalyst, 5-HMF electrooxidation can occur via direct oxidation or indirect oxidation mechanism, with 6-electron transfer leading to the formation of FDCA.[2e,11c,12b,44b,50] During the in direct oxidation, the applied potential is used to directly drive the electrooxidation of 5-HMF, while the valence state of the metal catalyst remains unchanged at the end of the reaction. A multi-step dehydrogenation via adsorbed hydroxyl species occurs, with the first pathway being the oxidation of an aldehyde group (Scheme 1), since the C-H bond cleavage would require a much higher energy barrier.[15-16] The second mechanism is the indirect oxidation of 5-HMF. In this mechanism, the applied potential leads to a change in the valence state of the electrocatalyst, which acts as a redox mediator to drive the oxidation of 5-HMF. In our case, whilst indirect oxidation (Scheme 3, left-side) is more straightforward, we suggest that both direct and indirect oxidation could occur since the CV and XPS show the tendency of Ni to change the valence state as a function of the applied potential or chemical environment. Thus, the HMF oxidation on $Ni_{2-x}Co_xP$ ($0 \leq x \leq 2$) electrode materials is also driven by the $Ni_{1-x}Co_x(OH)_2/Ni_{1-x}Co_xOOH$ redox center,[44a,51c] and the presence of P in pristine phosphide materials enables regulating their electron transfer capacity. For the first time, with two different configurations of spectroelectrochemical studies using cyclic voltammetry and FTIRS chronoamperometry, the involvement of hydroxyl metal species ($Ni_{1-x}Co_x(OH)_2$) is clearly demonstrated, since 5-HMF electrooxidation starts only when these $Ni_{1-x}Co_x(OH)_2$ species are formed (E > 1V vs. RHE). Furthermore, the overall proton-coupled electron transfer (PCET) reaction is expressed by Equation (10). We postulate that upon the first PCET step of dehydrogenation of 5-HMF molecules, Ni-based active sites are likely to be occupied by organic adducts, while proton species are transferred to neighboring cobalt and phosphorus active sites (as in the case of HER). Thus, modulation of the electronic properties of nickel by neighboring cobalt and phosphorus improves the stability of Ni-based active sites against poisoning by organic intermediates, as shown in Figure 7a.

$$\mathrm{HMF} + 8\mathrm{OH}^- \rightarrow \mathrm{FDCA}\ [\text{carboxylate form}] + 6\mathrm{H_2O} + 6e^- \qquad (10)$$

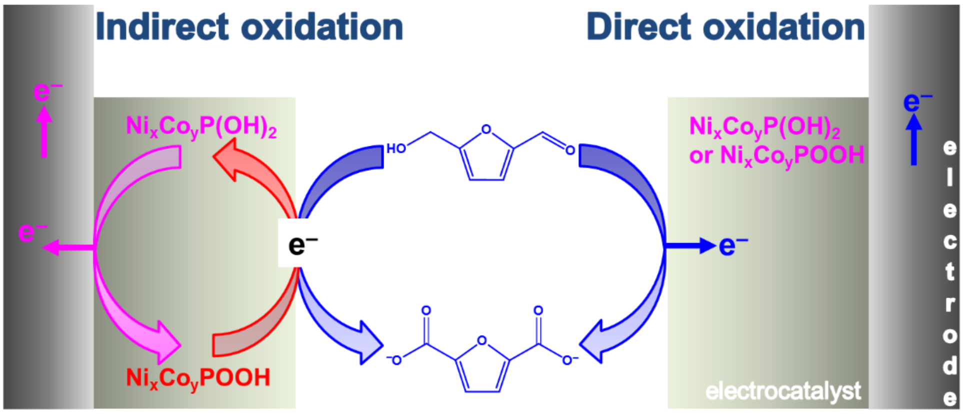

Scheme 3. Direct (right side) and indirect (left-side) electrooxidation mechanism pathways of 5-HMF into FDCA [carboxylate form] in alkaline media at the developed Ni_xCo_yP-based electrode materials.

3. Conclusion

In summary, this work has proposed a novel sacrificial synthesis strategy for the controlled *ex situ* phosphidation-free development of free-standing Ni_xCo_yP (as electrocatalytically active species) on nanostructured N,S,P-modified carbon networks (as support for electronic conduction and metal charge reduction) and illustrated the important role of microstructure refinement for the enhancement of physical and electrocatalytic properties. The synthesized nanostructured electrocatalysts were used as bifunctional electrode materials for the hydrogen evolution reaction (HER) and electrocatalytic conversion of organic biomass (5-HMF) to value-added 2,5-furandicarboxylic acid (FDCA). Extensive physicochemical (XRD, BET, SEM, STEM, EDX, Raman spectroscopy, XPS) and electrochemical characterization (CV, LSV), demonstrated that, despite the structural divergence of monometallic phosphides (Ni_2P (hexagonal), CoP (orthorhombic)), a single $Ni_{2-x}Co_xP$ hexagonal phase ($0 < x < 2$) is obtained for bimetallic phosphide materials, ruling out the hypothesis of segregated phases during carbothermal reduction (900 °C, N_2, 6 h). The coexistence of Ni, Co and P within the same crystalline structure in different atomic proportions leads to tunable geometric, electronic and electrocatalytic properties. To further investigate the electrooxidation mechanism of 5-HMF, we performed spectroelectrochemistry, chromatography (HPLC) and density functional theory

(DFT) studies, which confirm the selective electrooxidation of 5-HMF into FDCA. In particular, bulk electrolysis results show the ability to produce FDCA with a faradaic efficiency close to 100% for $Ni_{2-x}Co_xP$ when $0.5 \leq x \leq 1$, which is the best compromise in terms of current density and selectivity. According to XPS, the presence of P as negative sites ($P^{\delta-}$) can modify the electronic properties of Ni as positive sites ($Ni^{\delta+}$), while cobalt improves the chemical stability of nickel. These properties facilitate the dissociation of water during HER (where the Volmer step is the limiting reaction) and promote the formation of FDCA upon activation of the hydroxyl group of 5-HMF before the conversion of the two aldehyde functions to carboxylates. Further theoretical investigations on the effect of Co doping on the interaction with 5-HMF are currently underway, and detailed results will be presented in a future publication. Overall, this work presents an effective strategy for the simultaneous synthesis of an active electrocatalyst and its N,S,P-modified carbon support, and opens new avenues for the development of electrode materials for biomass electro-valorization.

4. Experimental Methods

Materials and Chemicals. ANI (100%, Alfa Aesar), H_3PO_4 (85%, VWR), APS [$(NH_4)_2S_2O_8$, 98%, Merck], $NiCl_2 \cdot 6H_2O$ (98%, Merck), $CoCl_2 \cdot 6H_2O$ (98%, Sigma Aldrich), KOH [99.98% (trace metal basis), Acros Organics], iPrOH (99.5%, Sigma Aldrich), Fumion FAA-3-SOLUT-10 (FuMA-Tech, Fuel Cell Store), alumina (Al_2O_3, ESCIL France), 5-(Hydroxymethyl)furfural (5-HMF, ≥99%, FG, Sigma-Aldrich), 2,5 furandicarboxylic acid (FDCA, 98%, Alfa Aesar), 2-formyl-5-furancarboxylic acid (FFCA, Sigma-Aldrich), 5-Hydroxymethyl-2-furancarboxylic acid (HFCA or HMFCA, ≥95%, Sigma-Aldrich), 2,5-Furandicarboxaldehyde (FDA or DFF, 97%, Sigma-Aldrich), acetonitrile (MeCN, 100%, Hoveywell) and methanol (MeOH, 100%, VWR) were used as received. Sustainion® X37-50 Grade RT (Fuel Cell Store) as hydroxide AEM was activated in 1 M KOH for 24 h prior to use. GDE (AvCarb MGL370, 370 µm thickness, Fuel Cell Store) was washed with iPrOH under medium shaking (orbital shaker RSLAB-7PRO, RS Lab) and dried in an oven (50 °C, 1 h) prior to use. Ultrapure Ar (grade 5.0, Air Liquide France) was used. A Milli-Q Millipore source produced ultrapure (18.2 MΩ cm at 20 °C).

Synthesis of Self-Supported Electrocatalysts. We have modified our early method of oxidative polymerization to target 5 compositions of Ni_xCo_yP (x:y = 1:0, 2:1, 1:1, 1:2, 0:1).[3a] A solution S1 (100 mL) was prepared by dissolving suitable amounts of $NiCl_2 \cdot 6H_2O$ and $CoCl_2 \cdot 6H_2O$ (see details in Table S1) in H_3PO_4 (0.5 M) that contains ANI (0.4 M), and transferred in a glass reactor (5 °C). Then, a second solution S2 (110 mL) was prepared by dissolving APS (0.5 M) in H_3PO_4 (0.5 M). Subsequently, S2 (100 mL) was added to S1 at 5 mL min^{-1} by a two-way syringe pump (KD Scientific). After 14 h under stirring, the solvent was removed using a rotary evaporator before drying the raw materials in an oven at 80 °C (overnight). Finally, these materials were calcined (N_2, 900 °C, 6 h) to yield the electrocatalysts. Temperature and duration were based on our previous study for PANI-based materials monometallic materials.[18b]

Physicochemical Characterization. PAnalytical Xpert-Pro diffractometer (40 kV, 40 mA, $Cu_{K\alpha}$ = 1.5406 Å) was used for XRD. N_2 adsorption-desorption measurements were conducted on Micromeritics ASAP 2020 instruments. A FEG JEOL 2200FS microscope (200 kV) was used for S/TEM-EDX. Hitachi S-4800 FEG microscope was used for SEM together with ZEISS EVOHD 15 microscope for EDX. Elementar vario MICRO cube was used for CHNS-O analysis and Agilent 5110 VDV spectrometer was used for Ni, Co and P analysis (ICP-OES). Raman spectroscopy was performed on a HORIBA Jobin Yvon LabRam HR8000UV Raman spectrometer (λ = 659.55 nm, LabSpec6 software) and the data were analyzed using pseudo-Voigt functions. XPS was conducted on a Kratos Axis Ultra DLD spectrometer (150 W, $Al_{K\alpha}$ = 1486.6 eV). Spectra [survey (1 eV per step, transition energy of 160 eV), high-resolution (0.1 eV per step, transition energy of 20 eV)] were calibrated using the C=C component C 1s at 284.6 eV. The Peaks fitting and the quantification (CASA XPS software) were carried out from the peak area after subtraction of background noise (Shirley) and correction with suitable sensitivity factors (Wagner).

Electrochemical Characterization. The experiments were performed in a conventional three-electrode setup using an AUTOLAB PGSTAT128N potentiostat (Metrohm) equipped with a linear SCAN250. A plate of glassy carbon (12.4 cm^2) and a mercury-mercury oxide electrode (MOE, Hg|HgO|KOH 1 M) were used as counter electrode and reference electrode, respectively. The potentials were scaled *versus* RHE through E(V vs RHE) = E(V vs MOE) + ΔE, where ΔE = 0.928 V (Figure S33). The working electrode consisted of a rotating disk electrode (RDE) tip of 5 mm (glassy carbon, 0.196 cm^2) polished with alumina slurries (1, 0.3 and 0.05 µm) followed by washing with ultrapure water (sonication in a water bath, 5 min). The catalytic ink was prepared by: (i) sonication (ice bath, 15 min) of iPrOH (400 µL) + H_2O (400 µL) + catalyst (11 mg), (ii) sonication (ice bath, 10 min) of the previous mixture plus Fumion (11 mg). Then, an aliquot of 4 µL was dropped onto the RDE (0.28 mg cm^{-2}, Ni+Co content represents 43-54 wt% depending on the composition (Table 1), and therefore a metallic charge of 0.12-0.15

mg_{Ni+Co} cm^{-2}) mounted on an inverted rotator shaft. Then, the rotator' speed was increased from 0 to 400 rpm for solvent evaporation (5-10 min) and obtaining a homogeneous thin-film of the catalytic layer. ECSA was estimated by the double-layer region method by plotting the absolute value of the double-layer charging current from CV (0.330-0.427 V vs RHE) for different scan rates (100-20 mV s^{-1}) and using the average specific capacitance of 35 µF cm^{-2} (although there is no standard value for the specific capacitance, which can vary from 11 to 130 µF cm^{-2}).[38a]

Spectroelectrochemistry. *In situ* FTIRS studies were performed with a home-made three-electrode electrochemical cell [µ-AUTOLAB type III potentiostat (Metrohm) and Bruker Vertex 80v spectrometer] in: (i) CV-FTIRS coupling [single potential alteration infrared spectra (SPAIRS)] by recording the reflectivity R_{Ei} of the electrode at different potentials Ei (step = 0.05 V) at 1 mV s^{-1}, (ii) CA-FTIRS coupling by recording a spectrum every Δt = 3 min when the electrode is poised at 1.42 V vs RHE. As the working electrode, 6 µL of the above catalytic ink was deposited onto a glassy carbon (7 mm diameter), which was pressed against a CaF_2 window to obtain a thin layer of the outgassed solution [KOH (1 M) + 5-HMF (0.1 M)]. The estimated loading is 0.21 mg cm^{-2} (Ni+Co content represents 43-54 wt% depending on the composition (Table 1), and therefore a metallic charge of 0.09-0.11 mg_{Ni+Co} cm^{-2}). The counter electrode was a large-area glassy carbon (>2 cm^2), and Hg|HgO|KOH 1 M was the reference electrode.

Electrolysis. Bulk electrolysis was made in a temperature-controlled and compartmentalized H-type cell. The working electrode was GDE (20 mm high, 25 mm width, 370 µm thickness) with enough space on the top for electrical wiring. The catalytic ink was prepared as above using iPrOH (400 µL), H_2O (400 µL), catalyst (50 mg), Fumion (40 mg), and drop-casting 101 µL onto each side (metal loading of 0.54-0.68 mg_{Ni+Co} cm^{-2}). A large-area glassy carbon plate (>20 cm^2) served as the counter electrode. The activated hydroxide AEM (see above) separated the working electrode compartment [anolyte: KOH (1 M) + 5-HMF (0.1 M), 35 mL] to that of the counter electrode compartment [catholyte: KOH (1 M), 35 mL]. The reference electrode (Hg|HgO|KOH 1 M) was in the working electrode compartment. A SP-150 potentiostat (Biologic Science Instruments, France) was used. The bulk electrolysis was performed at an applied potential of E_{appl} = 1.42 V vs RHE (iR-drop uncorrected) for 2 h. A volume of 500 µL was sampled from the working electrolyte every 30 min for HPLC analysis (see below). The HMF-to-FDCA faradaic efficiency (FE_{FDCA}(%)) was determined by Equation (11).

$$FE_{FDCA}\,(\%) = \frac{6 \times C_{FDCA}[mol\,L^{-1}] \times V[L] \times F[96485\,C\,mol^{-1}]}{Q_{ox}[C]} \times 100 \qquad (11)$$

Where F is the Faradaic constant, C_{FDCA} is the concentration of FDCA, V is the volume of the working electrode compartment and Q_{ox} is the total electrical charge.

Long-term stability test with the representative Ni_xCo_yP electrocatalyst (loaded onto GDE (10 mm high, 10 mm width, 370 µm thickness) under the same conditions except for the use of the galvanostatic method with two-electrode chronopotentiometry at an applied current of |I| = 20 mA (corresponding to a current density |j| of 10 mA cm^{-2}) to avoid complete oxidation of 5-HMF (3.5 mmol) during the 13.36 h tested (lesser than 36 h required for the full HMF-to-FDCA conversion, assuming 100% faradaic efficiency for the 6 electrons transferred, Equation (10)). A reference electrode (RHE, MiniHydroFlex®, Bio-Logic) was inserted in each compartment to follow the evolution of each electrode potential, positive electrode (anode, electrooxidation of 5-HMF, KOH (1 M) + 5-HMF (0.1 M), 45 mL) and negative electrode (cathode, HER, KOH (1 M), 35 mL). A multi-channel VSP-3e potentiostat (Biologic Science Instruments) was used to record the electrode potentials the anode (E_a) and cathode (E_c). We report in Figure S36 the detailed experimental set-up.

HPLC. The reaction products were analyzed by HPLC (Dionex ICS-1000). The analysis conditions were inspired by the seminal procedure developed by Kokoh and his colleagues:[46] (i) using an Atlantis dC18 Column (5 µm, 4.6×150 mm, Waters), (ii) the eluent was prepared by adding 900 mL of H_2SO_4 of pH 2.19 to a mixture of 50 mL acetonitrile and 50 mL methanol, (iii) the flow rate was 0.6 mL min^{-1}, (iv) the injection volume was 25 µL, and (v) the column temperature was 20 °C. Based on the UV−vis spectra of Figure S24 (stock solutions in 1 M KOH and diluted by the above eluent), the UV-vis detector wavelength was poised at $\lambda = 265$ nm for products analysis and establishing the calibration curves by external standards of expected products (Scheme 1).

Computational Methods.

DFT calculations were performed using the Vienna Ab initio Simulation Package (VASP).[52] The projected augmented wave method (PAW)[53] was applied and the electron exchange and correlation energies were calculated within the generalized gradient approximation with the Perdew-Burke-Ernzerhof (GGA-PBE) functional.[54] The optimization of structures was done when the force tolerance was lower than 0.01 eV/Å and the energy difference was lower than 10^{-6} eV. The cutoff energy was set as 400 eV. Spin-polarization was also included throughout our calculations. To study the reaction intermediates, $Ni_2P(111)$ surface slab was cut from optimized Ni_2P bulk of P-62m space group with a = b = 5.88 Å, and c = 3.37 Å (Figure S35). The 2x2- slab was formed by six atomic layers, for which, the bottom two layers were fixed o bulk parameters. The adsorbed gas molecules and the top four surface layers were allowed to relax. The adsorption energies of molecular or deprotonated 5-HMF molecule were calculated following the Equation (12).

$$E_{adsorption} = E_{molecule+surface} - E_{tot,molecule} - E_{tot,surface} \tag{12}$$

Where $E_{molecule+surface}$ is the total energy of the adsorbed system, $E_{tot,molecule}$ is the energy of the 5-HMF in gas phase and $E_{tot,surf}$ is the total energy of the bare Ni_2P surface.

Supporting Information

Supporting Information is available from the Wiley Online Library or from the author.

Acknowledgements

This work was partially funded by CNRS Energy unit (project PEPS21-CALEX4H2) and LabEx CheMISyst (ANR-10-LABX-05-01). This work was performed using HPC resources from GENCI-IDRIS (Grant 2023-[A0130807369]).

Conflict of Interest

The authors declare no conflict of interest

Data Availability Statement

The data that support the findings of this study are included in the published article and its Supplementary Information. Other data that support the findings of this study are available from the corresponding authors upon reasonable request.

Received: ((will be filled in by the editorial staff))
Revised: ((will be filled in by the editorial staff))
Published online: ((will be filled in by the editorial staff))

References

[1] a) Y. Sun, J. Miao, X. Fan, K. Zhang, T. Zhang, *Small Struct.* **2024**, *5*, 2300576; b) G. Yang, Y. Jiao, H. Yan, C. Tian, H. Fu, *Small Struct.* **2021**, *2*, 2100095; c) T. Wang, L. Tao, X. Zhu, C. Chen, W. Chen, S. Du, Y. Zhou, B. Zhou, D. Wang, C. Xie, P. Long,

W. Li, Y. Wang, R. Chen, Y. Zou, X.-Z. Fu, Y. Li, X. Duan, S. Wang, *Nat. Catal.* **2022**, *5*, 66.

[2] a) H. Xu, J. Bi, T. Sang, W. Wang, J. Hao, Z. Li, *Chem. Commun.* **2023**, *59,* 8440; b) H. Liu, J. Li, Y. Zhang, R. Ge, J. Yang, Y. Li, J. Zhang, M. Zhu, S. Li, B. Liu, L. Dai, W. Li, *Chem. Eng. J.* **2023**, *473,* 145397; c) D. Chen, H. Bai, J. Zhu, C. Wu, H. Zhao, D. Wu, J. Jiao, P. Ji, S. Mu, *Adv. Energy Mater.* **2023**, *13,* 2300499; d) K. Chang, D. T. Tran, J. Wang, K. Dong, S. Prabhakaran, D. H. Kim, N. H. Kim, J. H. Lee, *Appl. Catal. B: Env.* **2023**, *338*, 123016; e) H. Wang, C. Li, J. An, Y. Zhuang, S. Tao, *J. Mater. Chem. A* **2021**, *9*, 18421.

[3] a) H. Wei, F. Gu, Y. Wang, J. Hao, W. Zhu, Z. Zhuang, *ChemElectroChem* **2023**, *10*, e202300426; b) J. Zhang, K. Hou, Q. Yao, C. Wu, M. Huang, L. Guan, *Int. J. Hydrogen Energy* **2019**, *44*, 11684.

[4] a) J. Ma, A. Habrioux, C. Morais, A. Lewera, W. Vogel, Y. Verde-Gómez, G. Ramos-Sanchez, P. B. Balbuena, N. Alonso-Vante, *ACS Catal.* **2013**, *3*, 1940; b) J. Ma, A. Habrioux, N. Guignard, N. Alonso-Vante, *J. Phys. Chem. C* **2012**, *116*, 21788; c) J. W. Ma, A. Habrioux, Y. Luo, G. Ramos-Sanchez, L. Calvillo, G. Granozzi, P. B. Balbuena, N. Alonso-Vante, *J. Mater. Chem. A* **2015**, *3*, 11891.

[5] a) Q. Li, X. Luan, Z. Xiao, W. Xiao, G. Xu, Z. Li, Z. Wu, L. Wang, *Inorg. Chem.* **2023**, *62*, 9687; b) P. Yang, F. Liu, X. Zang, L. Xin, W. Xiao, G. Xu, H. Li, Z. Li, T. Ma, J. Wang, Z. Wu, L. Wang, *Adv. Energy Mater.* **2024**, *14,* 2303384; c) Z. Wu, Q. Li, G. Xu, W. Jin, W. Xiao, Z. Li, T. Ma, S. Feng, L. Wang, *Adv. Mater.* **2024**, *36,* 2311018; d) M. S. A. Sher Shah, G. Y. Jang, K. Zhang, J. H. Park, *EcoEnergy* **2023**, *1*, 344.

[6] C. A. Downes, K. M. Van Allsburg, S. A. Tacey, K. A. Unocic, F. G. Baddour, D. A. Ruddy, N. J. LiBretto, M. M. O'Connor, C. A. Farberow, J. A. Schaidle, S. E. Habas, *Chem. Mater.* **2022**, *34*, 6255.

[7] K. Mondal, N. Sathithsuksanoh, S. B. Lalvani, *SN Applied Sciences* **2020**, *2*, 2155.

[8] C. Jing, J. Ma, Q. Sun, Y. Li, X. Tang, F. Ling, Y. Wang, W. Zhang, X. Zhou, Y. Zhang, *CrystEngComm* **2023**, *25*, 1941.

[9] G. E. Ayom, M. D. Khan, S. C. Masikane, F. M. de Souza, W. Lin, R. K. Gupta, N. Revaprasadu, *Sustainable Energy Fuels* **2022**, *6*, 1319.

[10] L. Wang, Z. Wang, L. Chu, Z. Huang, M. Yang, G. Wang, *Int. J. Hydrogen Energy* **2024**, *64*, 830.

[11] a) D. S. Corrigan, M. J. Weaver, *J. Electroanal. Chem. Interf. Electrochem.* **1988**, *241,* 143; b) S. Barwe, J. Weidner, S. Cychy, D. M. Morales, S. Dieckhöfer, D. Hiltrop, J. Masa, M. Muhler, W. Schuhmann, *Angew. Chem. Int. Ed.* **2018**, *57*, 11460; c) H. Zhang, R. Zhang, W. Zhang, B. Gu, Q. Tang, Q. Cao, W. Fang, *Appl. Catal. B: Env.* **2023**, *330*, 122670.

[12] a) S. P. Verevkin, V. N. Emel'yanenko, E. N. Stepurko, R. V. Ralys, D. H. Zaitsau, A. Stark, *Ind. Eng. Chem. Res.* **2009**, *48*, 10087; b) Y. Kwon, K. J. P. Schouten, J. C. van der Waal, E. de Jong, M. T. M. Koper, *ACS Catal.* **2016**, *6*, 6704.

[13] P. Patel, D. Schwartz, X. Wang, R. Lin, O. Ajao, A. Seifitokaldani, *ACS Sustainable Chem. Eng.* **2022**, *10*, 4206.

[14] A. A. Rosatella, S. P. Simeonov, R. F. M. Frade, C. A. M. Afonso, *Green Chem.* **2011**, *13*, 754.

[15] a) B. Liu, J. Greeley, *J. Phys. Chem. C* **2011**, *115*, 19702; b) A. C. Garcia, M. J. Kolb, C. van Nierop y Sanchez, J. Vos, Y. Y. Birdja, Y. Kwon, G. Tremiliosi-Filho, M. T. M. Koper, *ACS Catal.* **2016**, *6*, 4491; c) Y. Holade, H. Guesmi, J.-S. Filhol, Q. Wang, T. Pham, J. Rabah, E. Maisonhaute, V. Bonniol, K. Servat, S. Tingry, D. Cornu, K. B. Kokoh, T. W. Napporn, S. D. Minteer, *ACS Catal.* **2022**, *12*, 12563.

[16] a) Z. Yang, S. Wang, C. Wei, L. Chen, Z. Xue, T. Mu, *Energy Environ. Sci.* **2024**, *17*, 1603; b) L. Wei, T. Sheng, J.-Y. Ye, B.-A. Lu, N. Tian, Z.-Y. Zhou, X.-S. Zhao, S.-G. Sun, *Langmuir* **2017**, *33*, 6991; c) T. Ishimoto, H. Kazuno, T. Kishida, M. Koyama, *Solid State Ionics* **2014**, *262*, 328; d) A. Caglar, D. Düzenli, I. Onal, I. Tezsevin, O. Sahin, H. Kivrak, *Int. J. Hydrogen Energy* **2020**, *45*, 490.

[17] M. Coronas, Y. Holade, D. Cornu, *Materials* **2022**, *15*, article number: 4336.

[18] a) Y. Holade, Z. H. Kavousi, M. Ghorbanloo, N. Masquelez, S. Tingry, D. Cornu, *Chem. Commun.* **2023**, *59*, 47; b) R. Djara, Y. Holade, A. Merzouki, M.-A. Lacour, N. Masquelez, V. Flaud, D. Cot, B. Rebiere, A. van der Lee, J. Cambedouzou, P. Huguet, S. Tingry, D. Cornu, *Front. Chem.* **2020**, *8*, Article 385.

[19] a) Z. Ge, B. Fu, J. Zhao, X. Li, B. Ma, Y. Chen, *J Mater Sci* **2020**, *55*, 14081; b) A.-L. Wang, J. Lin, H. Xu, Y.-X. Tong, G.-R. Li, *J. Mater. Chem. A* **2016**, *4*, 16992; c) J. F. Callejas, C. G. Read, C. W. Roske, N. S. Lewis, R. E. Schaak, *Chem. Mater.* **2016**, *28*, 6017; d) J.-X. Feng, S.-Y. Tong, Y.-X. Tong, G.-R. Li, *J. Am. Chem. Soc.* **2018**, *140*, 5118; e) J. Chen, J. Liu, J.-Q. Xie, H. Ye, X.-Z. Fu, R. Sun, C.-P. Wong, *Nano Energy* **2019**, *56*, 225; f) Y. Shi, B. Zhang, *Chem. Soc. Rev.* **2016**, *45*, 1529.

[20] a) J. Li, H. Zheng, C. Xu, Z. Su, X. Li, J. Sun, *Inorg. Chem.* **2021**, *60*, 1624; b) D. O. Mazur, O. O. Pariiska, Y. I. Kurys, V. G. Koshechko, V. D. Pokhodenko, *J. Electrochem. Soc.* **2024**, *171*, 076506.

[21] a) H.-T. Kwon, J.-H. Kim, K.-J. Jeon, C.-M. Park, *RSC Adv.* **2014**, *4*, 43227; b) H. Okamoto, *J. Phase Equilib. Diffus.* **2010**, *31*, 200.

[22] C. Du, L. Yang, F. Yang, G. Cheng, W. Luo, *ACS Catal.* **2017**, *7*, 4131.

[23] a) P. Strasser, S. Koh, T. Anniyev, J. Greeley, K. More, C. Yu, Z. Liu, S. Kaya, D. Nordlund, H. Ogasawara, M. F. Toney, A. Nilsson, *Nat. Chem.* **2010**, *2*, 454; b) D. Kumar, *Prog. Mater. Sci.* **2023**, *136*, 101106.

[24] a) J. Schwan, S. Ulrich, V. Batori, H. Ehrhardt, S. R. P. Silva, *J. Appl. Phys.* **1996**, *80*, 440; b) V. Perazzolo, C. Durante, R. Pilot, A. Paduano, J. Zheng, G. A. Rizzi, A. Martucci, G. Granozzi, A. Gennaro, *Carbon* **2015**, *95*, 949.

[25] E. Luo, M. Xiao, J. Ge, C. Liu, W. Xing, *J. Mater. Chem. A* **2017**, *5*, 21709.

[26] a) B. Devi, R. R. Koner, A. Halder, *ACS Sustainable Chem. Eng.* **2019**, *7*, 2187; b) J. Zhang, R. Cui, X. a. Li, X. Liu, W. Huang, *J. Mater. Chem. A* **2017**, *5*, 23536.

[27] R. S. Wagner, W. C. Ellis, *Appl. Phys. Lett.* **1964**, *4*, 89.

[28] M. G. Han, S. S. Im, *Polymer* **2000**, *41*, 3253.

[29] a) X. Wu, B. Yang, Z. Li, L. Lei, X. Zhang, *RSC Adv.* **2015**, *5*, 32976; b) V. S. Sumi, L. Elias, M. J. Deepa, S. M. A. Shibli, *Dalton Trans.* **2020**, *49*, 11628.

[30] a) R. M. Ferrizz, R. J. Gorte, J. M. Vohs, *Catal Lett* **2002**, *82*, 123; b) X. Yin, H. Dong, G. Sun, W. Yang, A. Song, Q. Du, L. Su, G. Shao, *Int. J. Hydrogen Energy* **2017**, *42*, 11262.

[31] a) C. Sun, H. Wang, J. Ren, X. Wang, R. Wang, *Nanoscale* **2021**, *13*, 13703; b) J. Wu, X. Ge, Z. Li, D. Cao, J. Xiao, *Electrochim. Acta* **2017**, *252*, 101.

[32] a) V. S. Sumi, M. A. Sha, S. R. Arunima, S. M. A. Shibli, *Electrochim. Acta* **2019**, *303*, 67; b) L. Xie, R. Zhang, L. Cui, D. Liu, S. Hao, Y. Ma, G. Du, A. M. Asiri, X. Sun, *Angew. Chem. Int. Ed.* **2017**, *56*, 1064.

[33] a) K. Wang, R. Zhao, Z. Wang, X. Zhang, A. Ouyang, C. Zhou, W. Zhou, X. Tan, Y. Chu, *Appl. Surf. Sci.* **2023**, *626*, 157218; b) M. Yang, Q. Huang, X. Luo, J. Jiang, Q. Wang, C. Chen, C. Zheng, X. Liu, G. Deng, *Mater. Lett.* **2021**, *303*, 130482.

[34] B. Rezaei, A. R. T. Jahromi, A. A. Ensafi, *Int. J. Hydrogen Energy* **2017**, *42*, 16538.

[35] a) C. Zhang, S. M. Park, *J. Electrochem. Soc.* **1987**, *134*, 2966; b) M. S. E. Houache, E. Cossar, S. Ntais, E. A. Baranova, *J. Power Sources* **2018**, *375*, 310.

[36] D. A. J. Rand, R. Woods, *J. Electroanal. Chem. Interf. Electrochem.* **1972**, *36*, 57.

[37] A. Habrioux, W. Vogel, M. Guinel, L. Guetaz, K. Servat, B. Kokoh, N. Alonso-Vante, *Phys. Chem. Chem. Phys.* **2009**, *11*, 3573.

[38] a) C. C. L. McCrory, S. Jung, J. C. Peters, T. F. Jaramillo, *J. Am. Chem. Soc.* **2013**, *135*, 16977; b) N. L. Fröhlich, J. J. J. Eggebeen, M. T. M. Koper, *Electrochim. Acta* **2024**, *494*, 144456.

[39] a) X. Deng, M. Li, Y. Fan, L. Wang, X.-Z. Fu, J.-L. Luo, *Appl. Catal. B: Env.* **2020**, *278*, 119339; b) R. Chen, J. Wu, Y. Zhu, X. Wu, Z. Li, S. Yin, *ACS Appl. Nano Mater.* **2024**, *7*, 7605; c) S. Liang, L. Pan, T. Thomas, B. Zhu, C. Chen, J. Zhang, H. Shen, J. Liu, M. Yang, *Chem. Eng. J.* **2021**, *415*, 128864.

[40] a) S. Wang, X. Gao, X. Hang, X. Zhu, H. Han, W. Liao, W. Chen, *J. Am. Chem. Soc.* **2016**, *138*, 16236; b) R. Ma, Y. Zhou, F. Wang, K. Yan, Q. Liu, J. Wang, *Mater. Today Energy* **2017**, *6*, 173.

[41] M. Chatenet, J. Benziger, M. Inaba, S. Kjelstrup, T. Zawodzinski, R. Raccichini, *J. Power Sources* **2020**, *451*, 227635.

[42] a) V. Jose, E. Edison, W. W. Manalastas, Jr., S. Sreejith, J. M. Vianney Nsanzimana, M. Srinivasan, J.-M. Lee, *ACS Appl. Mater. Interfaces.* **2019**, *11*, 39798; b) H. Liu, X. Ma, H. Hu, Y. Pan, W. Zhao, J. Liu, X. Zhao, J. Wang, Z. Yang, Q. Zhao, H. Ning, M. Wu, *ACS Appl. Mater. Interfaces.* **2019**, *11*, 15528; c) Y. Jia, L. Zhu, H. Pan, Y. Liao, Y. Zhang, X. Zhang, Z. Jiang, M. Chen, K. Wang, *Appl. Surf. Sci.* **2022**, *580*, 152314; d) C. Wang, J. Jiang, T. Ding, G. Chen, W. Xu, Q. Yang, *Advanced Materials Interfaces* **2016**, *3*, 1500454.

[43] J. Staszak-Jirkovský, Christos D. Malliakas, Pietro P. Lopes, N. Danilovic, Subrahmanyam S. Kota, K.-C. Chang, B. Genorio, D. Strmcnik, Vojislav R. Stamenkovic, M. G. Kanatzidis, N. M. Markovic, *Nat. Mater.* **2016**, *15*, 197.

[44] a) L. Guo, X. Zhang, L. Gan, L. Pan, C. Shi, Z.-F. Huang, X. Zhang, J.-J. Zou, *Adv. Sci.* **2023**, *10*, 2205540; b) Z. Zhou, Y.-n. Xie, L. Sun, Z. Wang, W. Wang, L. Jiang, X. Tao, L. Li, X.-H. Li, G. Zhao, *Appl. Catal. B: Env.* **2022**, *305*, 121072; c) H. Zhou, Y. Ren, B. Yao, Z. Li, M. Xu, L. Ma, X. Kong, L. Zheng, M. Shao, H. Duan, *Nat. Commun.* **2023**, *14*, 5621; d) N. Jiang, B. You, R. Boonstra, I. M. Terrero Rodriguez, Y. Sun, *ACS Energy Lett.* **2016**, *1*, 386; e) A. B. Abderrahmane, S. Tingry, D. Cornu, Y. Holade, *Adv. Energy Sustainability Res.* **2024**, *5*, 2300302.

[45] C. Lv, S. Guo, T. Yang, K. Li, *Chem. Eng. J.* **2020**, *399*, 125601.

[46] A. Al Baradii, K. B. Kokoh, H. Huser, C. Lamy, J. M. Léger, *Electrochim. Acta* **1999**, *44*, 2779.

[47] a) D. H. Nam, B. J. Taitt, K. S. Choi, *ACS Catal.* **2018**, *8*, 1197; b) Z. Yang, B. Zhang, C. Yan, Z. Xue, T. Mu, *Appl. Catal. B: Env.* **2023**, *330*, 122590.

[48] D. J. Chadderdon, L. Xin, J. Qi, Y. Qiu, P. Krishna, K. L. More, W. Li, *Green Chem.* **2014**, *16*, 3778.

[49] Y. Holade, A. B. Engel, K. Servat, T. W. Napporn, C. Morais, S. Tingry, D. Cornu, K. B. Kokoh, *J. Electrochem. Soc.* **2018**, *165*, H425.

[50] A. R. Poerwoprajitno, L. Gloag, J. Watt, S. Cychy, S. Cheong, P. V. Kumar, T. M. Benedetti, C. Deng, K. H. Wu, C. E. Marjo, D. L. Huber, M. Muhler, J. J. Gooding, W. Schuhmann, D. W. Wang, R. D. Tilley, *Angew. Chem.-Int. Edit.* **2020**, *59*, 15487.

[51] a) M. T. Bender, Y. C. Lam, S. Hammes-Schiffer, K.-S. Choi, *J. Am. Chem. Soc.* **2020**, *142*, 21538; b) M. Fleischmann, K. Korinek, D. Pletcher, *J. Chem. Soc., Perkin Trans. 2* **1972**, 1396; c) D. A. Giannakoudakis, J. C. Colmenares, D. Tsiplakides, K. S. Triantafyllidis, *ACS Sustainable Chem. Eng.* **2021**, *9*, 1970.

[52] a) G. Kresse, J. Furthmüller, *Phys. Rev. B* **1996**, *54*, 11169; b) G. Kresse, J. Furthmüller, *Comput. Mater. Sci.* **1996**, *6*, 15.

[53] G. Kresse, D. Joubert, *Phys. Rev. B* **1999**, *59*, 1758.

[54] J. P. Perdew, K. Burke, M. Ernzerhof, *Phys Rev Lett* **1996**, *77*, 3865.

We present a solid-state, phosphidation-free strategy for the synthesis of Ni_xCo_yP multi-metal phosphide materials in N,S,P-modified nanostructured carbon networks generated alongside Ni_xCo_yP as self-supporting electrocatalysts. This one-step carbothermal reduction under an inert atmosphere enhances the particle-support interaction and tunes the electronic and geometric interactions between P, Ni and Co to promote the adsorption/desorption of reactants and/or intermediates during electrocatalytic reactions.

Sarra Knani, Myriam Tauk, Perla Hajjar, Marie-Agnès Lacour, Masoud Shahrokhi, Christine Canaff, Cláudia Morais, Sophie Morisset, Patrice Huguet, Didier Cot, Bertrand Rebiere, Erwan Oliviero, Julien Cambedouzou, Mikhael Bechelany, Sophie Tingry, K. Boniface Kokoh, Teko W. Napporn, Hazar Guesmi*, David Cornu, and Yaovi Holade*

Phosphidation-free Synthesis of Ni_xCo_yP on Nanostructured N,S,P-Doped Carbon Networks as Self-Supported Multifunctional Electrocatalysts